ACS APPLIED MATERIALS & INTERFACES

www.acsami.org

Research Article

Blood-Glucose-Depleting Hydrogel Dressing as an Activatable Photothermal/Chemodynamic Antibacterial Agent for Healing Diabetic Wounds

Wei Zhu,[$] Ya-Qin Liu,[$] Pei Liu, Jun Cao, Ai-Guo Shen,[*] and Paul K. Chu[*]

Cite This: *ACS Appl. Mater. Interfaces* 2023, 15, 24162−24174

Read Online

ACCESS | Metrics & More | Article Recommendations | Supporting Information

ABSTRACT: Poorly healing and nonhealing diabetic wounds are challenging to treat as the rapid growth of bacteria due to the high local glucose content can lead to persistent inflammation and poor angiogenesis. Herein, a smart hydrogel dressing composed of 3,3′,5,5′-tetramethylbenzidine/ferrous ion/Pluronic F-127/glucose oxidase (TMB/Fe^{2+}/PF127/GOx) is designed and demonstrated to consume blood glucose while accelerating wound healing by generating antibacterial agents *in situ*. The loaded GOx degrades blood glucose to provide hydrogen peroxide (H_2O_2) and gluconic acid to support the Fe^{2+}-based Fenton reaction, and the generated hydroxyl radical (·OH) facilitates the oxidation of TMB. The color change from colorless to green caused by the oxidation of TMB in the blood glucose range between 1 and 10 mM can be monitored visually. Simultaneously, this process induced chemodynamic therapy (CDT) by the specific generation of hydroxyl radical (·OH) for killing bacteria. Moreover, the oxidized TMB shows strong absorption in the near infrared (NIR) region so that NIR light can be converted into heat efficiently for photothermal therapy (PTT). As a result, nearly 100% of *Staphylococcus aureus* and *Escherichia coli* are killed by synergistic PTT/CDT, and the infected skin wounds undergo complete repair along with downregulation of interleukin-6 (IL-6) and upregulation of the vascular endothelial growth factor (VEGF) and matrix metallopeptidase-2 (MMP-2). Different from traditional wound dressings that can give rise to secondary injury, the excellent thermosensitive properties arising from the sol/gel phase transition render the hydrogel dressing materials injectable, self-reparable, and removable on demand. The multifunctional hydrogel with hypoglycemic, chemodynamic, photothermal, antibacterial, and on-demand thermosensitive properties has immense potential in the treatment of diabetic wounds.

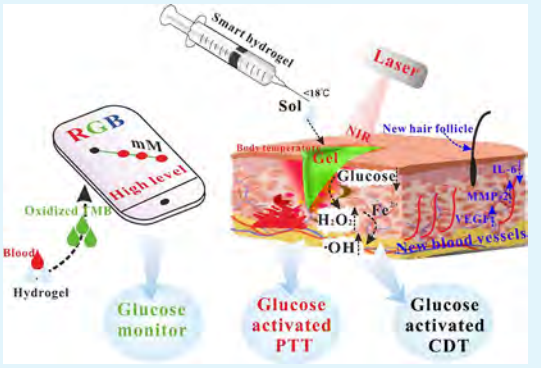

KEYWORDS: *diabetic wound, smart hydrogel dressing, glucose depleting, activatable antibacterial agent, photothermal therapy, chemodynamic therapy*

1. INTRODUCTION

Nonhealing diabetic wounds that are challenging to treat constitute one of the common complications for diabetic patients due to acute and repetitive bacterial infection and even nontraumatic amputation.[1−4] A high level of blood glucose is known to be an important factor delaying wound healing because it provides a nutrient for bacterial and viral reproduction.[5−7] In addition, prolonged hyperglycemia can lead to the accumulation of advanced glycation end-products (AGEs) that reduce the secretion of multiple growth factors and in turn lead to continuous inflammatory and poor angiogenesis.[8−10]

Dressings are basic to wound treatment for diabetic patients.[11,12] It has been shown that a moist environment *in vivo* promotes the migration and reproduction of epidermal cells and it is significantly better than wound healing in a dry environment.[13] Traditional dressings including a dry gauze, oil gauze, cotton pad, and bandage play a passive role to isolate wounds but impose no direct effects on wound healing.[14] To facilitate "wet healing", a series of modern new dressings such as water colloid and alginate have been developed.[15,16] Hydrogels as a class of materials with three-dimensional network properties have also been used in wound dressings due to favorable swelling, biocompatibility, hygroscopicity, moisture retention, and similarity to biological soft tissues.[17−21] However, they are difficult to remove with a potential risk of secondary injury on the wound. To facilitate the on-demand change of fresh dressings, thermosensitive hydrogels based on the liquid to solid to liquid transition by controlling the temperature are attractive for the treatment of

Received: March 15, 2023
Accepted: April 28, 2023
Published: May 11, 2023

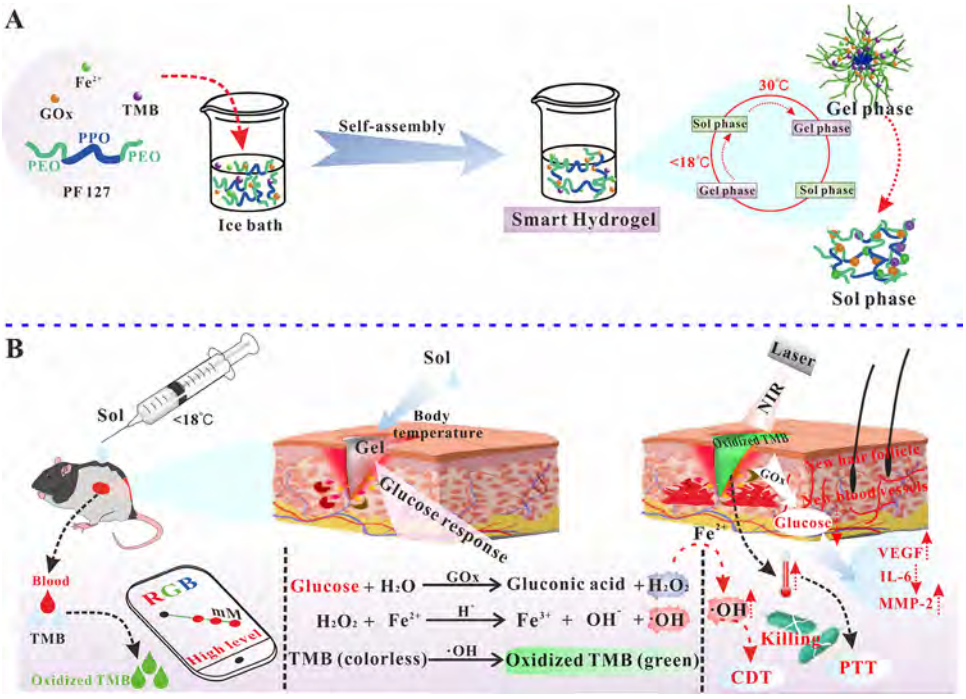

Figure 1. Schematic diagram of the preparation and application of TMB/Fe^{2+}/PF127/GOx hydrogel. (A) Preparation of the TMB/Fe^{2+}/PF127/GOx hydrogel. (B) The schematic diagram of blood glucose monitoring, nontraumatic adhesion and detachment within temperature control, and glucose responsive mechanism of the TMB/Fe^{2+}/PF127 hydrogel and its application in diabetic wound healing. CDT represents chemodynamic therapy; PTT represents photothermal therapy; and IL-6, VEGF, and MMP-2 represent interleukin-6, vascular endothelial growth factor, and matrix metalloproteinase-2, respectively.

diabetic wounds because of the injectability to cover large-area and irregular wounds.[22,23]

To accelerate wound healing in diabetic patients, modern dressings with enhanced mechanical, biological, and chemical properties are required. They must also carry drugs such as those for blood glucose regulation and antibacterial activity.[24−29] To downregulate blood glucose in local wounds, dressing strategies such as patches for insulin release and carriers with glucose oxidase (GOx) for *in situ*/*in vivo* consumption of blood glucose have been proposed.[23,30−32] Moreover, antibiotics are commonly administered to treat wound infections, but drug resistance and biofilms can adversely affect the healing of diabetic wounds.[33−36] The photonic-mediated approach such as photothermal antibacterial therapy has emerged to be an alternative to antibiotics. Photothermal therapy (PTT) agents such as noble metal nanoparticles (Au, Cu), transition metal chalcogenides (CuS, WS_2), and carbon-based nanomaterials (carbon nanotubes, graphene) have been proposed.[37] Nevertheless, the high local temperature caused by PTT can interfere with other bioactive drugs such as GOx, and therefore, better PTT agents are important.[38] Moreover, photothermal antibacterial efficacy might be restricted to some extent by the low efficiency of photothermal conversion and inhomogeneous distribution of hyperthermia. Chemodynamic therapy (CDT) based on the Fenton reaction to catalyze H_2O_2 to generate highly toxic ROS for efficient killing bacteria, displaying merits of diabetic wound's specificity with cascade catalytic blood glucose, and depth independence.[39,40] Therefore, developing a glucose-activated multimodal CDT/PTT agent with reducing glucose and monitoring the glucose level simultaneously is imperative for accelerating diabetic wound healing.[41−45]

Herein, the Pluronic F-127 (PF127) thermosensitive hydrogel dressing combining the capabilities of colorimetric glucose sensing and glucose-activated chemodynamic/photothermal functions is designed and demonstrated for simultaneous glucose monitoring and antimicrobial therapy to accelerate diabetic wound healing. As shown in Figure 1A, 3,3′,5,5′-tetramethylbenzidine (TMB) is used as an intermediate bridge to synthesize the TMB/Fe^{2+}/PF127/glucose oxidase (GOx) hydrogel. TMB has been used as the chromogenic substrate in glucose colorimetric analysis due to the noncarcinogenicity and nonmutagenicity.[46,47] The colorless TMB is converted into oxidized TMB when the TMB/Fe^{2+}/PF127/GOx hydrogel is applied as the wound dressing for diabetic patients (Figure 1B). Meanwhile, the microenvironment is broken down by GOx into gluconic acid and hydrogen peroxide (H_2O_2), and H_2O_2 forms the hydroxyl free radical (·OH) in the presence of Fe^{2+} in the hydrogel so that the glucose concentration can be measured with the aid of a smartphone by monitoring the change of the green color.[48] Moreover, the oxidized TMB exhibits strong photothermal effects upon NIR laser irradiation to accomplish bacteria killing.[49]

2. EXPERIMENTAL SECTION

2.1. Materials. The PF127 powder, 3,3′,5,5′-tetramethylbenzidine (TMB), and hydrogen peroxide (H_2O_2) were purchased from Sigma-Aldrich Co., Ltd. (U.S.A.), and the commercial hydrogel (Tegaderm hydrogel 91110) supplied by 3M was used in the positive control group. Glucose oxidase (Gox) was obtained from Shanghai Yuanye Bio-Technology Co., Ltd. (Shanghai, China), and ferrous chloride ($FeCl_2·7H_2O$), sodium chloride (NaCl), glucose, tryptone, and yeast extract were provided by Sinopharm Chemical Reagent Co., Ltd. (Shanghai, China). The mouse embryonic fibroblast NIH/3T3 cells (ATCC CRL-1658) obtained from ATCC (Manassas, VA, USA)

https://doi.org/10.1021/acsami.3c03786
ACS Appl. Mater. Interfaces 2023, 15, 24162−24174

were cultured in the Dulbecco's modified Eagle's medium with a high glucose concentration (DMEM-HG, Sangon Biotech, Shanghai). The fetal bovine serum (FBS), Calcein-AM, and propidium iodide (PI) were bought from Sangon Biotech (Shanghai, Beijing), and 18 MΩ·cm deionized water purified by the Millipore-Q purification system (Millipore, Bedford, MA) was used in the experiments.

2.2. Preparation and Optimization of the PF127 Hydrogel. PF127 powder (1.5, 2.0, and 2.5 g) was added to 10 mL of precooled pure water and stirred at a low temperature for 6 h to obtain the PF127 hydrogels with different weight fractions of 15, 20, and 25%, respectively. The phase-transition temperature of the PF127 hydrogels with different weight fractions was measured by placing 1 mL of the PF127 hydrogel in a glass vial in a constant temperature water bath from 10 to 40 °C. The hydrogel with the proper weight fraction used in the subsequent experiments was characterized by ultraviolet spectrophotometry (Shimadzu, UV2550) and ZEISS field-emission scanning electron microscopy (FE-SEM).

2.3. Synthesis of the TMB/Fe^{2+}/PF127 Hydrogel and Optimization of the Fe^{2+} Concentration. The TMB/Fe^{2+}/PF127 hydrogel was prepared at a low temperature with a TMB concentration of 8 mg/mL and a weight fraction of PF127 of 20%. The TMB/Fe^{2+}/PF127 hydrogels were prepared in solutions with different Fe^{2+} solutions of 2, 1, 0.1, 0.05, 0.01, and 0.005 mg/mL, and then 1 mL of the TMB/Fe^{2+}/PF127 hydrogel was mixed with 100 μL of H_2O_2 with a concentration of 10 mM. The color change was monitored by ultraviolet spectrophotometry and the smart phone app "Colorshot". The TMB/Fe^{2+}/PF127 hydrogel with the optimal concentration of Fe^{2+} was characterized by ultraviolet spectrophotometry and FE-SEM.

2.4. Rheological Evaluation. The dynamic rheological properties of the PF127 hydrogel and TMB/Fe^{2+}/PF127 hydrogels were determined according to a previous method. The TA AR2000 rheometer equipped with hydrogel disks with a diameter of 40 mm and a Peltier heating system was used. The samples were thermally balanced for 1 min prior to the measurement, and the storage modulus (G') and loss modulus (G'') were determined at an oscillation frequency of 6.283 rad/s and constant strain of 1%. The temperature was varied from 4 to 40 °C, and the samples were covered with sealed caps to reduce evaporation during the measurement.

2.5. Self-Healing. The self-healing properties of the TMB/Fe^{2+}/PF127 hydrogel were determined optically and quantitatively. In the optical visualization experiment, the TMB/Fe^{2+}/PF127 hydrogel was cut gently from the center with a blade, and the hydrogel with cracks was put in close proximity for a certain time to observe self-healing by a Canon camera. The self-healing behavior was studied by applying strain sweeps from 1 to 500% strain at 37 °C for three cycles, and the time interval was set as 100 s. The G' and G'' values were recorded every 6 s at an angular frequency of 6.283 rad/s.

2.6. Stability of the TMB/Fe^{2+}/PF127 Hydrogel. To evaluate the stability of the hydrogel, the color change of the mixture of TMB/Fe^{2+}/PF127 hydrogel and H_2O_2 solution was observed by a mobile phone for a week. The changes in the green values were also analyzed by Colorshot.

2.7. Quantitative Determination of H_2O_2. A series of H_2O_2 solutions with different concentrations were added to the TMB/Fe^{2+}/PF127 hydrogel for quantitative evaluation. The concentrations were 10, 8, 6, 4, 2, 1, 0.5, 0.4, 0.3, 0.2, and 0.1 mM. The color change was observed by ultraviolet spectrophotometry and Colorshot. The Origin software was used to establish the linear regression plots by plotting the green value or the OD_{652} of mixture versus H_2O_2 concentrations.

2.8. Quantitative Determination of Glucose. GOx catalyzes the oxidative decomposition of glucose and is essential for the detection of glucose. Briefly, 10 μL of GOx with different concentrations (1, 5, 10, 15, and 20 mg/mL) and 90 μL of the glucose solution (10 mM) were added to 1 mL of the TMB/Fe^{2+}/PF127 hydrogel. The color changes were monitored by a smart phone and ultraviolet spectrophotometry. In the glucose detection, 10 μL of GOx (10 mg/mL) was added to 1 mL of the TMB/Fe^{2+}/PF127 hydrogel, and glucose concentrations of 10, 8, 6, 4, 2, 1, 0.5, 0.4, 0.3, 0.2, and 0.1 mM were used. The color changes were captured by a smart phone, and the absorption spectra were acquired by ultraviolet spectrophotometry. Furthermore, blood samples of db/db mice were further used for checking its sensing capacity of glucose. The blood of five diabetic mice was provided by Wuhan Pinuofei Biological Co., Ltd. The initial blood glucose value was measured by a commercial Yuyue glucose meter. Blood samples containing different glucose concentrations of 2, 4, 6, 8, and 10 mM were prepared by adding pure medium (Dulbecco's modified Eagle's medium with no glucose) for diluting blood glucose. The TMB/Fe^{2+}/PF127/GOx hydrogel (100 μL) was mixed with 9 μL of blood samples with different glucose concentrations. Pictures of color changes were taken by a smart phone, and the Origin software was used to construct the linear regression plots by plotting the green value or the OD_{652} of the mixture versus the glucose concentrations.

2.9. Photothermal Properties of the TMB/Fe^{2+}/PF127/GOx Hydrogel. To explore the optimal laser power, 90 μL of glucose (10 and 2 mM) was added to 1 mL of the TMB/Fe^{2+}/PF127/GOx hydrogel. After 5 min, 300 μL of the mixture was placed in a 500 μL tube for irradiation for 5 min by the 808 nm NIR laser using different power values of 0.5, 1.0, and 2 W. An infrared thermal imaging camera (EasIR-4, Guide Infrared Limited Company, Wuhan, China) was employed to record the temperature of samples before and after laser irradiation. The photothermal effects of the glucose-activated TMB/Fe^{2+}/PF127/GOx hydrogels were determined with the 808 nm NIR laser. In brief, 1.0 mL of the TMB/Fe^{2+}/PF127/GOx hydrogel and 90 μL of the glucose solution (10, 8, 6, 4, 2, or 1 mM) were mixed, and after 5 min, 300 μL of the mixture was put in a 0.5 mL tube and irradiated with the 808 nm NIR laser with a laser power of 2 W for 10 min. The temperature was recorded every 20 s by the infrared thermal imaging camera. At the same time, the changes were also captured by a smart phone.

2.10. Bacteria Culture. *Escherichia coli* (*E. coli*) DSM 4230 and *Staphylococcus aureus* (*S. aureus*) ATCC 91093 were provided by the China Centre for Type Culture Collection (CCTCC). The bacterial strains were cultured in the sterile Luria–Bertani broth at 37 °C until the bacteria concentration was proper, and then the bacteria were mixed with the hydrogel and irradiated with the NIR laser. The sterilizing rate was determined by the plating and culturing method.

2.11. *In Vitro* Antibacterial Evaluation. *S. aureus* (Gram-positive bacteria) and *E. coli* (Gram-negative bacteria) were used to evaluate the photothermal sterilization performance of the TMB/Fe^{2+}/PF127/GOx hydrogel activated by glucose. The samples were divided into the control group, TMB/Fe^{2+}/PF127/GOx hydrogel group, TMB/Fe^{2+}/PF127/GOx hydrogel with 10 mM of glucose group, and TMB/Fe^{2+}/PF127/GOx hydrogel with 2 mM of glucose group. Briefly, 100 μL of bacterial solution was mixed with 900 μL of the materials. The mixture (300 μL) was placed in a 0.5 mL tube for 5 min and illuminated by the 808 nm laser for 10 min. The mixture was smeared evenly on the surface of LB agar with a coating rod, and the bacteria were counted after culturing for 24 h at 37 °C. The bactericidal effects were evaluated by the live/dead staining assay. The mixtures of the bacteria and different materials were centrifuged, and the bacteria were resuspended in the PBS solution. The bacterial suspension was further treated with Calcein-AM (10×10^{-6} M) and PI (10×10^{-6} M) for 15 min. The fluorescence images of the living and dead bacteria were captured by a confocal microscope (Olympus).

2.12. Cytocompatibility of the TMB/Fe^{2+}/PF127/GOx Hydrogels. The *in vitro* cytotoxicity of the TMB/Fe^{2+}/PF127/GOx hydrogel and PF127 hydrogel was evaluated by the Cell Counting Kit-8 (CCK-8) using mouse embryonic fibroblast cells (NIH-33 cells). The cells were cultured on 96-well plates at 37 °C for 24 h to reach a certain concentration. Afterward, the cell culture medium was discarded and replaced with the TMB/Fe^{2+}/PF127/GOx hydrogel and PF127 hydrogel, respectively. The cell viability was determined from fluorescence images acquired by confocal microscopy. The NIH-3T3 cells without the TMB/Fe^{2+}/PF127/GOx hydrogel and bare PF127 hydrogel were the positive control.

https://doi.org/10.1021/acsami.3c03786
ACS Appl. Mater. Interfaces 2023, 15, 24162–24174

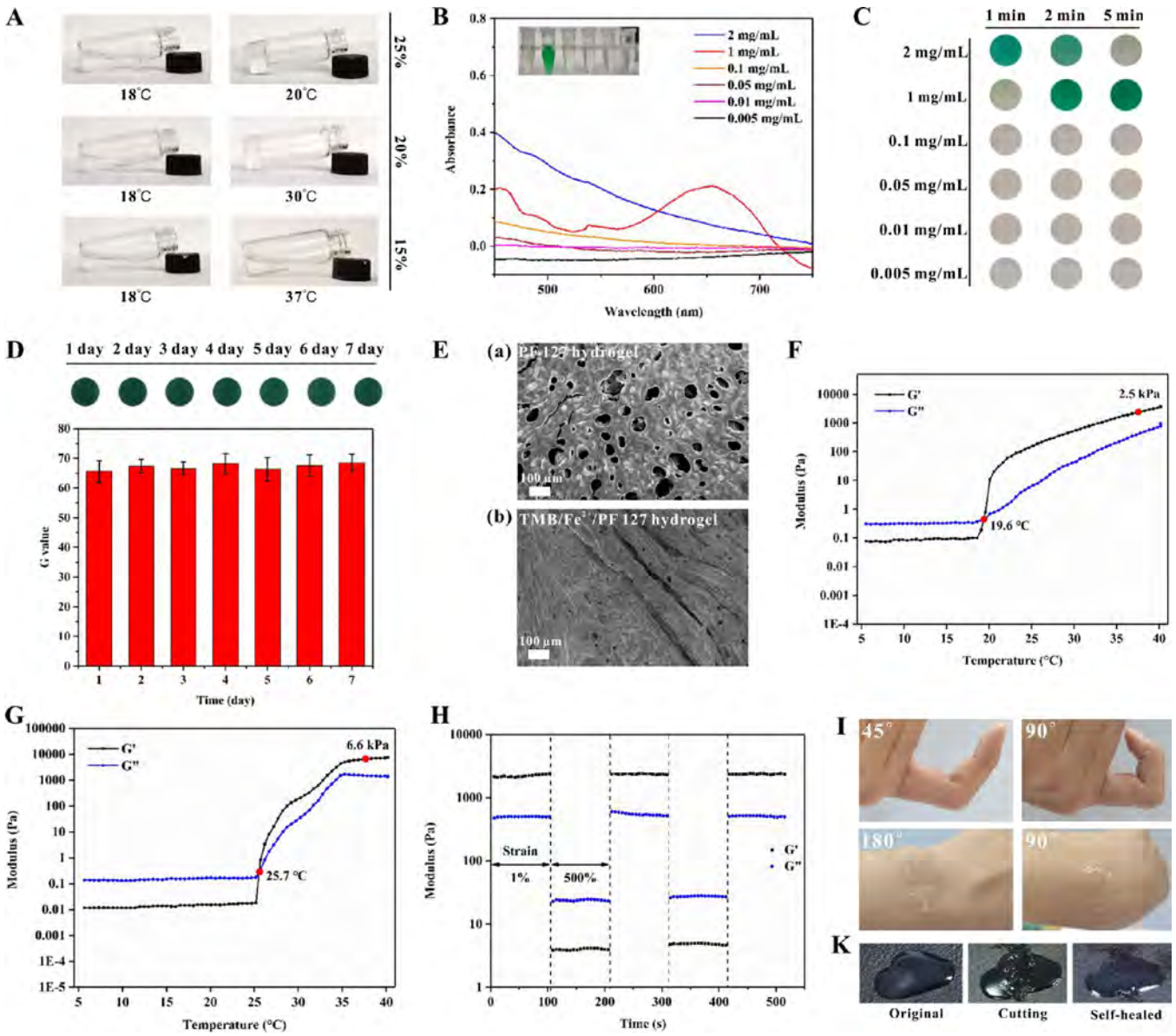

Figure 2. (A) Phase transition at different temperatures for the PF127 hydrogels with different concentrations of 25, 20, and 15%. (B) UV−vis spectra of the products of H_2O_2 and TMB/Fe^{2+}/PF127 hydrogel containing different concentrations of Fe^{2+}. (C) Images of the product of H_2O_2 and TMB/Fe^{2+}/PF127 hydrogel containing different concentrations of Fe^{2+}. (D) Stability of the TMB/Fe^{2+}/PF127 hydrogels for 7 days with the error bars derived from the standard deviations of three independent experiments. (E) FE-SEM images of the (a) PF127 hydrogel and (b) TMB/Fe^{2+}/PF127 hydrogel. (F) G' and G'' values of the TMB/Fe^{2+}/PF127 hydrogel for different temperatures. (G) G' and G'' values of the PF127 hydrogel for different temperatures. (H) Rheological properties of the TMB/Fe^{2+}/PF127 hydrogel when the alternate step strain is switched from 1 to 500%. (I) Pictures of the TMB/Fe^{2+}/PF127 hydrogel on the finger and wrist under different bending degrees. (K) Self-healing properties of the TMB/Fe^{2+}/PF127 hydrogel with the red dots corresponding to the phase transition temperature and G' value at 37 °C.

2.13. *In Vivo* Wound Healing Ability. The *in vivo* wound healing effects of the TMB/Fe^{2+}/PF127/GOx hydrogel were evaluated based on the full-thickness bacteria-infected wound model. The mice experiments were supported by Wuhan Pinuofei Biological Co., Ltd. Briefly, the db/db mice (30−40 g, 5−6 weeks old) provided by Wuhan Rat Bailey Biology Co., Ltd., were randomly divided into four groups (six mice in each group) including the control group, positive control group (Tegaderm film), TMB/Fe^{2+}/PF127/GOx hydrogel group, and TMB/Fe^{2+}/PF127/GOx hydrogel with NIR laser group. The mice were anesthetized with chloral hydrate, and the dorsal hair of the mice was removed. Round wounds with a diameter of 8 mm were made, and the suspension of *S. aureus* (50 μL, 1×10^8 CFU/mL) was placed in the wounds. The control group was treated with PBS, and the other groups were covered by the Tegaderm film and TMB/Fe^{2+}/PF127/GOx hydrogel, respectively. The wounds of the TMB/Fe^{2+}/PF127/GOx hydrogel with NIR laser group were irradiated with the NIR laser (2 W) for 10 min. After irradiation for 10 min, the mice were fed under normal conditions until the wound healed, and the hydrogels were replaced every 3 days. At the same time, wound regeneration was recorded by a smart phone, and the wound area was calculated by the screenshot software. The wounded skin tissues were harvested after 10 and 21 days to perform hematoxylin−eosin (H&E) staining and Masson's trichrome staining. After treatment for 21 days, the mice were euthanized, and the main organs including the heart, liver, spleen, lung, and kidney were harvested for analysis.

2.14. Histology and Immunohistochemistry. H&E staining and Masson's trichrome staining were conducted to study the histomorphological changes and collagen metabolism during wound regeneration in different phases. Briefly, 5 μm thick slices of the

https://doi.org/10.1021/acsami.3c03786
ACS Appl. Mater. Interfaces 2023, 15, 24162−24174

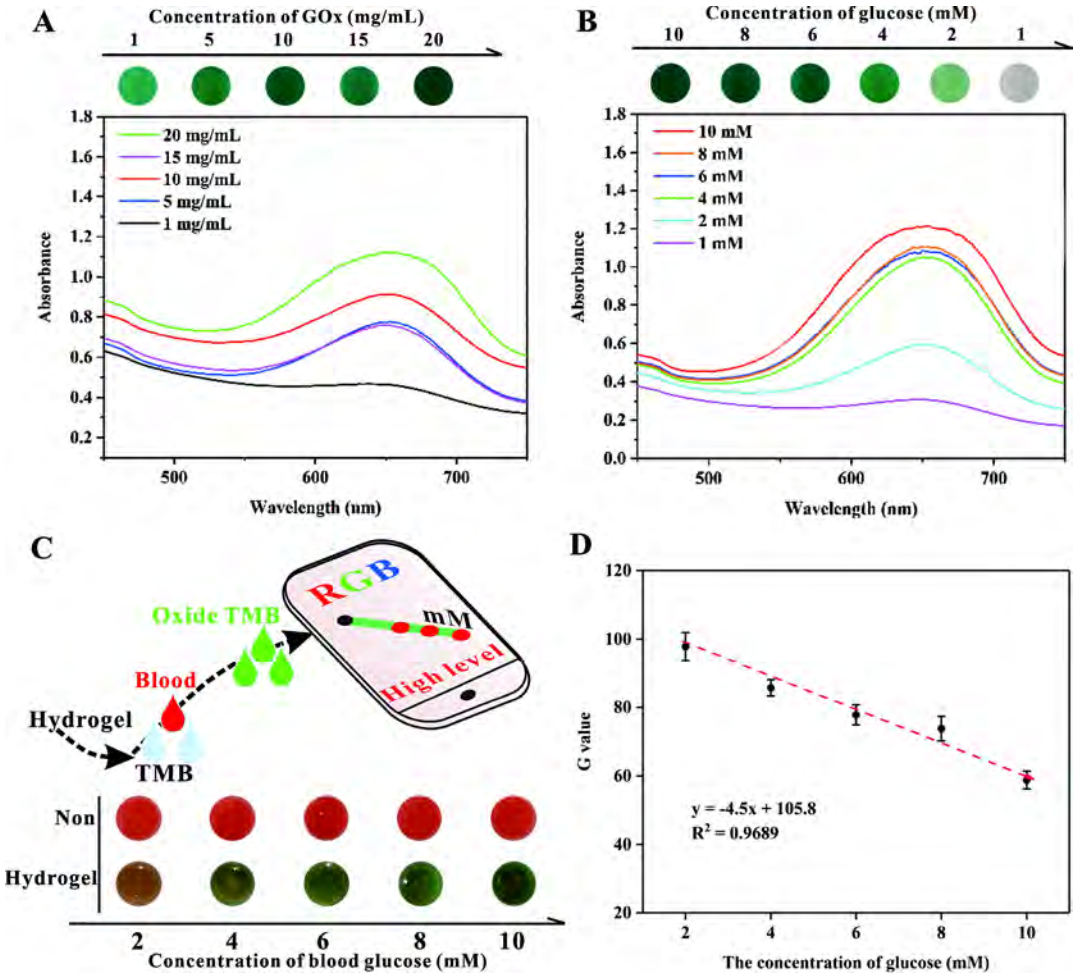

Figure 3. Detection ability of the TMB/Fe^{2+}/PF127/GOx hydrogel for glucose. (A) Concentration optimization of glucose oxidase. (B) UV−vis spectra of the products after the reaction in the glucose solutions with different concentrations and TMB/Fe^{2+}/PF127/GOx hydrogel. (C) Detection of blood glucose. Pictures of blood samples containing different concentrations of glucose (nonhydrogel) and the product after the reaction between the TMB/Fe^{2+}/PF127/GOx hydrogel and blood samples (hydrogel). (D) Calibration curve of glucose concentration versus green values of the products with the error bars derived from the standard deviations of three independent experiments.

regenerated wound tissues collected after 10 and 21 days were stained with H&E dye and Masson's trichrome staining kit. The histomorphological and collagen pictures were acquired on a microscope (IX53, Olympus, Japan). Immunofluorescence staining was performed with the IL-6, VEGF, and MMP-2 antibodies, respectively.

2.15. Statistical Analysis. All the experimental results were statistically analyzed and expressed as mean ± standard deviation (SD). The *t* test was used to determine the differences between two groups by the SPSS 18.0 software. The *P* value of 0.05 was the important reference to judge the significance level, and the results were labeled with different symbols to represent the data differences, for example, (*) for $P < 0.05$, (**) for $P < 0.01$, (***) for $P < 0.001$, and (****) for $P < 0.0001$.

3. RESULTS AND DISCUSSION

3.1. Preparation of the TMB/Fe^{2+}/PF127 Hydrogel. The amount of PF127 powder affects the phase transition temperature of the TMB/Fe^{2+}/PF127 hydrogel is optimized to ensure that the hydrogel functions at the human temperature.[50] As shown in Figure 2A, the phase transition temperature of the hydrogel decreases with PF127 concentration, and the 15% sample failed to change from the sol to gel state in the temperature range of 18 to 37 °C. When the amount of PF127 is increased to 20 and 25%, the TMB/Fe^{2+}/PF127 hydrogel changes to a gel state at 30 and 20 °C, respectively. Considering the compromise between the human temperature and reaction efficiency, the 20% TMB/Fe^{2+}/PF127 hydrogel is selected for the subsequent experiments.

The decomposition of H_2O_2 by Fe^{2+} to produce the hydroxyl free radical is a typical Fenton reaction.[51] Owing to the strong oxidation ability of the hydroxyl radical, the colorless TMB becomes green during oxidation, and so colorimetric sensing is appropriate. Because the concentration of Fe^{2+} influences the degree and rate of color change, the effects of different concentrations of Fe^{2+} are explored. As shown in Figure 2B,C, the colorless TMB/Fe^{2+}/PF127 hydrogel changes to green when the concentration of Fe^{2+} is increased to 1 mg/mL, and the absorbance at 652 nm goes up as well. The color change is quick, but fading occurs in a short time as the Fe^{2+} concentration is increased. It may be caused by the fast transformation of oxidized TMB for diimine with the excessive electron and high pH produced by the reaction of too much Fe^{2+} and H_2O_2 and further degradation.[52] The reaction time was studied, and as shown in Figure 2C and Figure S1, the absorbance at 652 nm increases gradually in the first 0−5 min and then stabilizes between 5 and 10 min. Hence, the optimal reaction time is set to be 5 min. The

https://doi.org/10.1021/acsami.3c03786
ACS Appl. Mater. Interfaces 2023, 15, 24162−24174

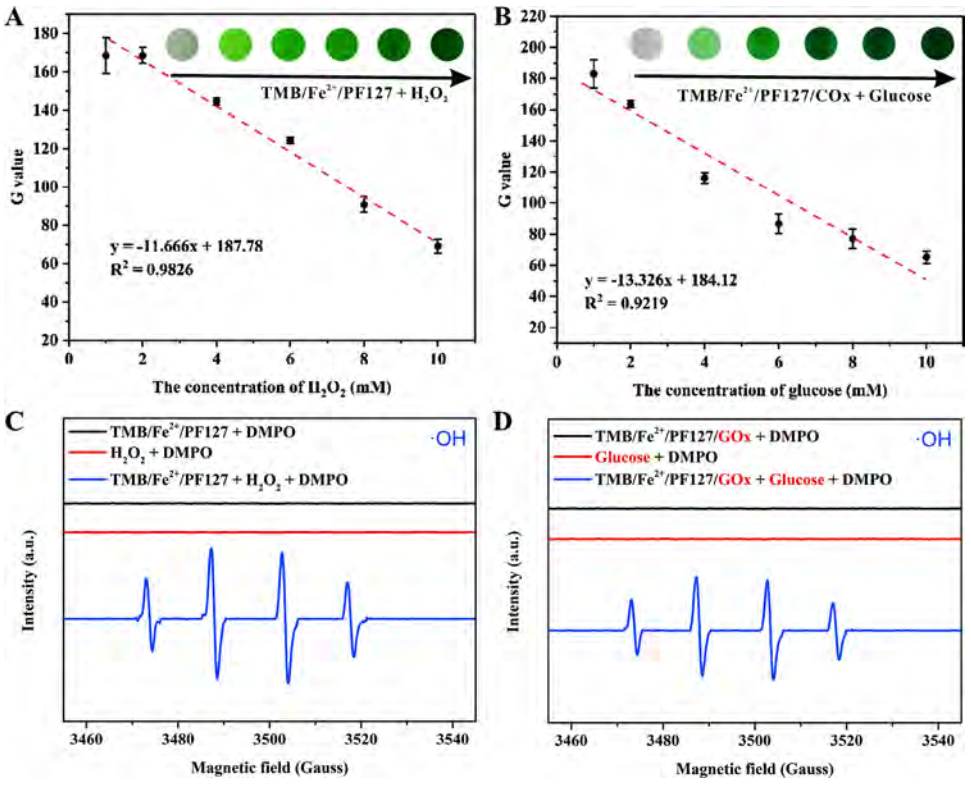

Figure 4. (A) Color pictures of reaction products between the TMB/Fe^{2+}/PF127 hydrogel and H_2O_2 solution and the calibration curve between the *G* value. (B) Color pictures of reaction products between TMB/Fe^{2+}/PF127/GOx hydrogel and glucose solution and the calibration curve between the *G* value. (C) ESR spectra of TMB/Fe^{2+}/PF127 induced ·OH generation with or without H_2O_2. (D) ESR spectra of TMB/Fe^{2+}/PF127/GOx induced ·OH generation with or without glucose.

quantitative response of the TMB/Fe^{2+}/PF127 hydrogel to H_2O_2 is a prerequisite to glucose monitoring. As shown in Figure S2, there are visual color differences after the TMB/Fe^{2+}/PF127 hydrogel reacts with H_2O_2 in the 1−10 mM concentration range with good linearity ($y = -11.666x + 187.78$, $R^2 = 0.9826$). As shown in Figure S3A, the absorbance at 652 nm increases gradually with H_2O_2 concentration, and a good linear correlation can be established for $y = 0.1622x + 0.3773$ with $R^2 = 0.9415$ (Figure S3B). The linear relationship observed by the color change is better than that of the UV−vis results, indicating that visual inspection is adequate and effective. However, monitoring becomes more difficult for the lower H_2O_2 concentration range of 0.1−0.5 mM (Figure S4). The stability of the TMB/Fe^{2+}/PF127 hydrogel is crucial to the accurate determination of the H_2O_2 concentration. Therefore, the color change of the TMB/Fe^{2+}/PF127 hydrogel is monitored during H_2O_2 addition by a smart phone for a week, and as shown in Figure 2D, good stability is attained.

3.2. Characterization of the PF127 and TMB/Fe^{2+}/PF127 Hydrogels. The PF127 and TMB/Fe^{2+}/PF127 hydrogels are characterized by field-emission scanning electron microscopy (FE-SEM) and UV−vis spectrophotometry. As shown in the FE-SEM images, the PF127 hydrogel has a porous structure with an average pore size of 50 μm (Figure 2E). Compared to the PF127 hydrogel, an ordered morphology and microfibrous structure with a smaller pore size are observed from the TMB/Fe^{2+}/PF127 hydrogel attributable to the coordination between Fe^{2+} and the hydroxyl group in PF127 and ensuing promoted cross-linking of hydrogels.[53] The UV−vis spectra (Figure S5) reveal stronger absorbance by the TMB/Fe^{2+}/PF127 hydrogel. The rheological tests reveal that the mechanical strength and self-healing ability are reflected by the changes in the storage modulus G' and loss modulus G'' with time and strain.[23] As shown in Figure 2F,G, after addition of TMB and Fe^{2+}, the phase transition temperature decreases to 19.6 °C in comparison with the PF127 hydrogel because of cross-linking of the hydrogel by coordination between Fe^{2+} and the hydroxyl group in PF127.[23]

To explore the self-healing ability of the TMB/Fe^{2+}/PF127 hydrogel, a continuous step strain test is performed. As shown in Figure 2H, as the continuous shear strain alternates between 1 and 500%, the stress of each segment is maintained for nearly 100 s. Under a lower shear strain of 1%, the hydrogel structure is stable, and G' is larger than G''. Under a higher shear strain of 500%, the hydrogel exhibits shear thinning characteristics with G'' being larger than G', G', and G'' changing synchronously with strain alternation. This process is repeatable, disclosing the excellent self-repairing ability. With the addition of Fe^{2+}, the elastic modulus improves, and the excellent self-repairing ability is maintained.[54]

The TMB/Fe^{2+}/PF127 hydrogels can be used on finger joints and wrists because of the excellent injectability and self-healing. As shown in Figure 2I, the finger and wrist can bend freely without resistance after application of the hydrogel, which continues to cover the finger and wrist at multiple different angles, boding well for wound dressings. After the TMB/Fe^{2+}/PF127 hydrogel is cut, it self-heals quickly as shown in Figure 2K, demonstrating the suitability for treatment of diabetic wounds.[22]

3.3. Preparation of the TMB/Fe^{2+}/PF127/GOx Hydrogel. Glucose monitoring and timely regulation are essential for

https://doi.org/10.1021/acsami.3c03786
ACS Appl. Mater. Interfaces 2023, 15, 24162−24174

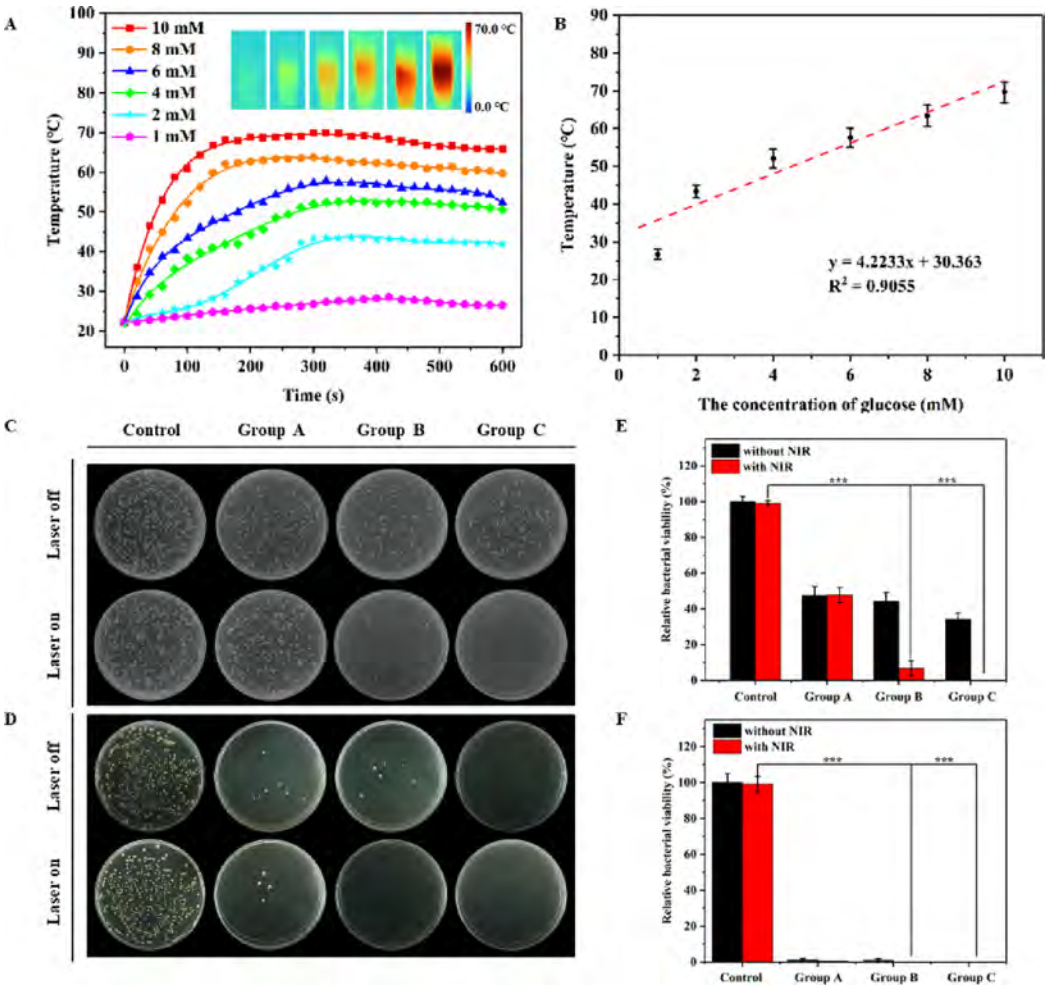

Figure 5. Photothermal and bactericidal properties of the TMB/Fe^{2+}/PF127/GOx hydrogel: (A) temperature variation at different time points during laser irradiation time for 10 min with the inset showing the infrared images of the product after irradiation for 4 min; (B) calibration curve of temperature versus glucose concentration after laser irradiation of 5 min with the error bars derived from the standard deviations of three independent experiments; (C) antibacterial evaluation of the TMB/Fe^{2+}/PF127/GOx hydrogel against *E. coli*; (D) antibacterial assessment of the TMB/Fe^{2+}/PF127/GOx hydrogel against *S. aureus*; (E) *E. coli* killed by the TMB/Fe^{2+}/PF127/GOx hydrogel; and (F) *S. aureus* killed by the TMB/Fe^{2+}/PF127/GOx hydrogel (*** representing $P < 0.001$ for highly significant differences).

diabetic wound management, and therefore, the concentration of glucose oxidase should be optimized. As shown in Figure 3A, an obvious color change and the largest absorbance are observed for a glucose oxidase concentration of 10 mg/mL, which is adopted in subsequent experiments. The reaction time is explored, and as shown in Figure S5, the TMB/Fe^{2+}/PF127/GOx hydrogel becomes darker gradually with time in the initial 5 min. The color becomes the darkest after 5 min, so 5 min is determined to be the optimal time.

3.4. Glucose Sensing by the TMB/Fe^{2+}/PF127/GOx Hydrogel. The TMB/Fe^{2+}/PF127/GOx hydrogel is mixed with solutions with different glucose concentrations, and as shown in Figure 3B, the TMB/Fe^{2+}/PF127/GOx hydrogel darkens gradually with glucose concentration. Additionally, the absorbance at 652 nm increases with glucose concentration in the 1−10 mM range. Similarly, the TMB/Fe^{2+}/PF127/GOx hydrogel shows no obvious change as the glucose concentration is increased from 0.1 to 0.5 mM, consistent with the results for H_2O_2 (Figure S6). Nonetheless, the excellent characteristics observed in the glucose range of 1−10 mM meet the requirements for diabetic patients.

To assess the effects on actual blood glucose, the mouse blood samples were treated with certain glucose concentrations. The actual blood glucose level of db/db mouse was detected as nearly 20 mM with three repetitions by the commercial meter (Figure S7). As shown in Figure 3C, the initial color of the blood samples containing different glucose concentrations is roughly the same. However, after adding the TMB/Fe^{2+}/PF127/GOx hydrogel, the color changes obviously. The color of the samples becomes darker (green) visually as the glucose concentration goes up (Figure 3C).[55] According to the smart phone data, a good linear correlation (R^2 = 0.9689) between the green value and blood glucose concentration is observed (Figure 3D), indicating that the TMB/Fe^{2+}/PF127/GOx hydrogel possessed a potential sensing capacity for local blood glucose in diabetic wounds.

3.5. Chemodynamic Property of the Glucose Activated TMB/Fe^{2+}/PF127/GOx Hydrogel. It is known that Fe^{2+} has excellent Fenton reaction activity and catalyzes the oxidation of TMB by hydrogen peroxide (H_2O_2), thereby forming abundant ·OH.[39,40] Interestingly, H_2O_2 was produced by the decomposition of glucose with GOx catalyzed.[39] Therefore, the generation of ·OH could be activated by

https://doi.org/10.1021/acsami.3c03786
ACS Appl. Mater. Interfaces 2023, 15, 24162−24174

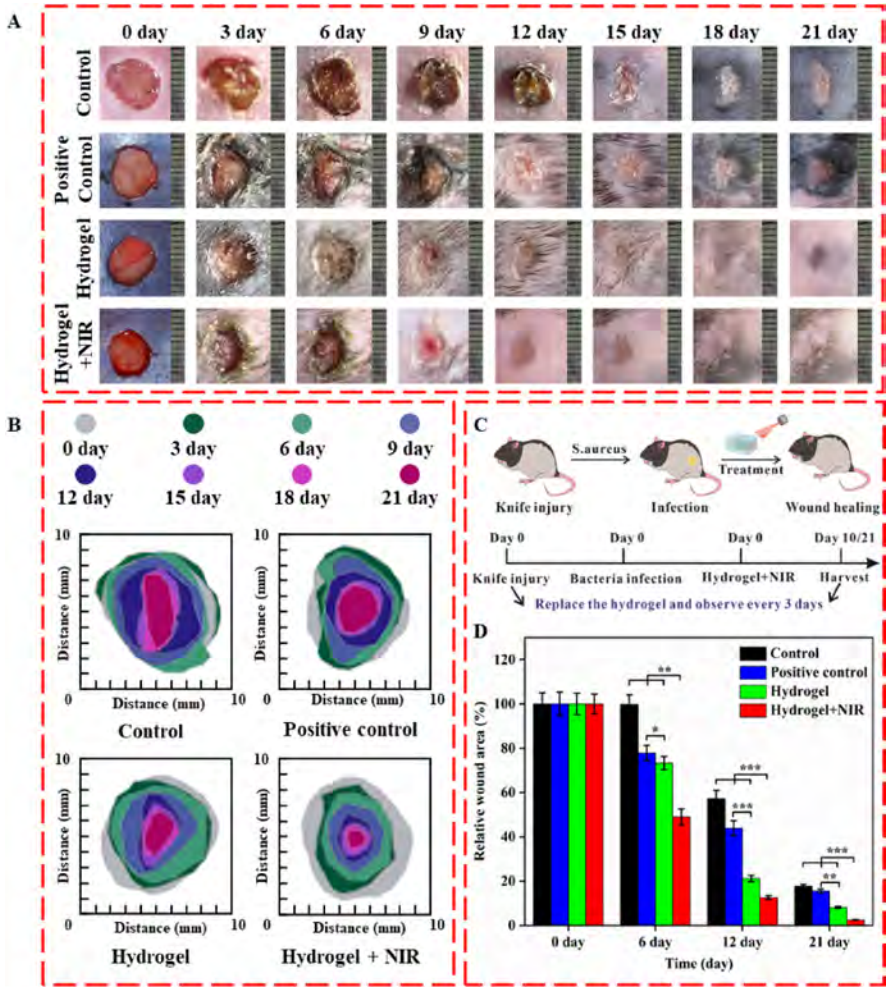

Figure 6. *In vivo* antibacterial assessment of the TMB/Fe^{2+}/PF127/GOx hydrogel: (A) photographs of the *S. aureus*-infected wounds after different treatments for 21 days; (B) traces of wound bed closure for 21 days for each treatment; (C) schematic diagram illustrating the timeline of the operation process; and (D) wound areas at different treatment time for each group (* represents $P < 0.05$, ** represents $P < 0.01$, and *** represents $P < 0.001$). The error bars are derived from the standard deviations of three independent experiments.

glucose with the TMB/Fe^{2+}/PF127/GOx hydrogel; meanwhile, the chemodynamic property is timely activated for killing bacteria. To explore the chemodynamic property of the TMB/Fe^{2+}/PF127 with H_2O_2 and TMB/Fe^{2+}/PF127/GOx hydrogel with glucose, colorimetric reaction of TMB and ESR spectroscopy were used to confirm the production of ·OH. As shown in Figure 4A,B, the color of the hydrogel gradually darkens with the increase of H_2O_2 and glucose concentration, and a good linear correlation was obtained by linear fitting of H_2O_2 and glucose concentration and the green value of the final products, corresponding to the results of glucose sensing (Figure 3B–D). As shown in the ESR spectra (Figure 4C,D), only when the TMB/Fe^{2+}/PF127 hydrogel, H_2O_2, and trapping agent (DMPO) or the TMB/Fe^{2+}/PF127/GOx hydrogel, glucose, and trapping agent (DMPO) coexisted could the ·OH signal appear. According to the above results, we speculated that the possible catalytic mechanism of the TMB/Fe^{2+}/PF127/GOx hydrogel was attributed to the transformation of glucose to H_2O_2 by GOx and immediate generation of ·OH after reacting with Fe^{2+}.[56−58]

3.6. Photothermal Properties of the Glucose-Activated TMB/Fe^{2+}/PF127/GOx Hydrogel. After reacting with blood glucose, the TMB/Fe^{2+}/PF127/GOx hydrogel possessed NIR photothermal property, which was attributed to the excellent NIR absorbance of OxTMB that transformed from glucose activatable TMB/Fe^{2+}/PF127/GOx hydrogel. As shown in Figure S8, after NIR laser irradiation for 5 min, no obvious temperature change is observed from the control group, PF127 hydrogel group, and TMB/Fe^{2+}/PF127/GOx hydrogel group, whereas the temperature increases significantly for the glucose-activated TMB/Fe^{2+}/PF127/GOx hydrogel in conjunction with a phase transition (Figure S9), demonstrating the potential for photothermal sterilization.[59]

To attain the best photothermal antibacterial ability, the photothermal effects of the TMB/Fe^{2+}/PF127/GOx hydrogel with 2 or 10 mM glucose are determined using different laser power values. After irradiation for 10 min at 1 and 2 W, the 10 mM temperature is above 43 °C, and the hydrogel changes from the solution to sol (Figures S10A,B). However, the 2 mM temperature reaches 43 °C only upon 2 W laser irradiation (Figures S11A,B). Hence, a laser power of 2 W is used in subsequent experiments. The 1−10 mM glucose-activated NIR photothermal effects are further investigated after laser irradiation for 10 min at 2 W. As shown in Figure 5A, the temperature increases with glucose concentration at the same time points, and the heating rates are positively associated with the glucose concentration. When the glucose concentration is 10 or 8 mM, the temperature of the TMB/Fe^{2+}/PF127/GOx

https://doi.org/10.1021/acsami.3c03786
ACS Appl. Mater. Interfaces 2023, 15, 24162−24174

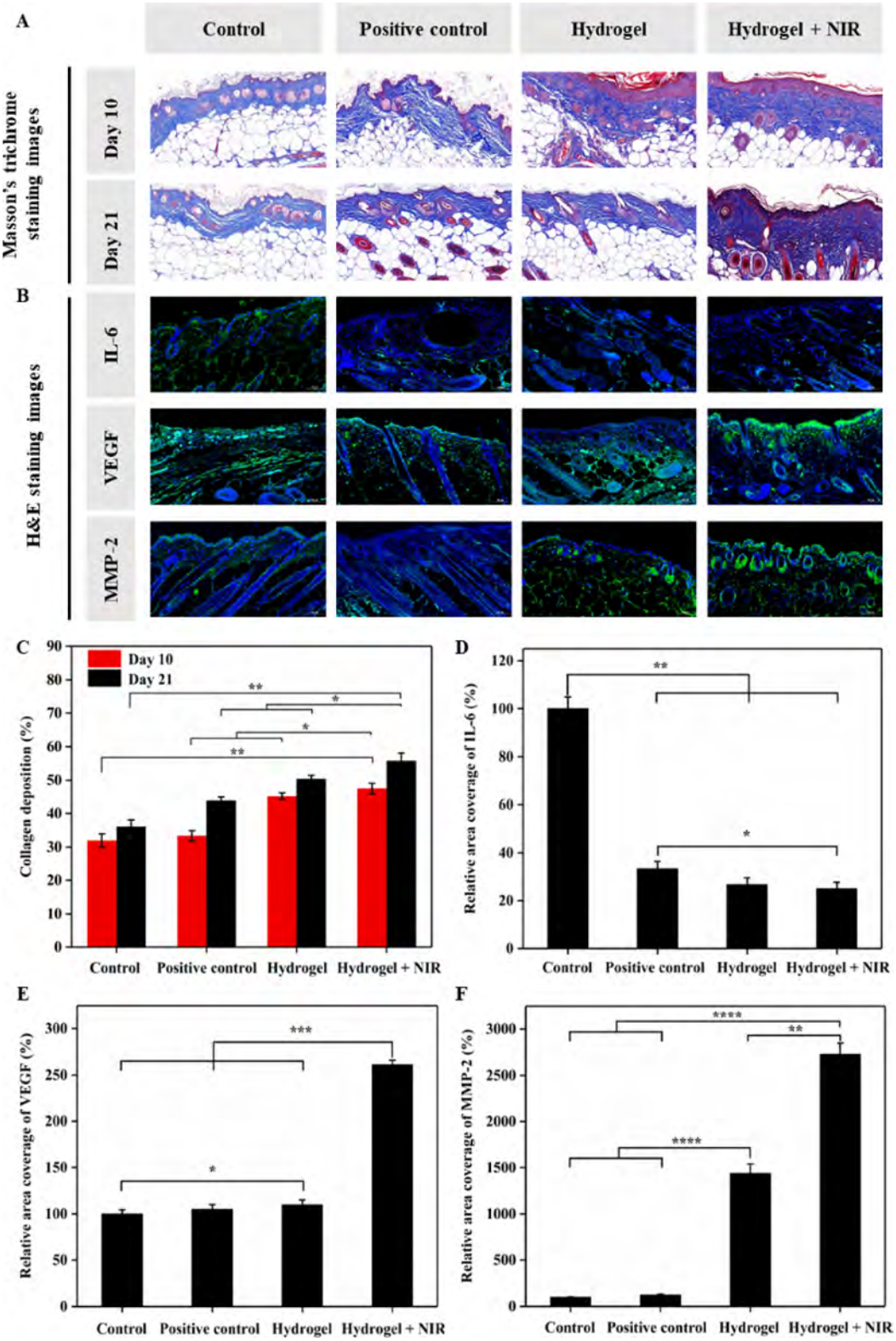

Figure 7. The TMB/Fe^{2+}/PF127/GOx hydrogel promoted diabetic wound healing *in vivo* via regulating cytokines. (A) Collagen deposition at the 10th and 21st days. (B) Immunofluorescence staining images of IL-6, VEGF, and MMP-2 on the 21st day. (C) Statistical data of the relative expression of collagen. (D) Statistical data of the relative expression of IL-6. (E) Statistical data of the relative expression of VEGF. (F) Statistical data of the relative expression of MMP-2. The error bars are derived from the standard deviations of three independent experiments.

hydrogel increases rapidly before 180 s and stabilizes. Upon further laser irradiation, the temperature tends to decrease at around 350 s because of photobleaching of organic molecules. The heating rate of the TMB/Fe^{2+}/PF127/GOx hydrogel is relatively small when the glucose concentration is 2−6 mM, and it reaches the highest temperature at about 300 s. Although the temperature shows a downward trend with irradiation time, it remains at about 43 °C, which can kill

https://doi.org/10.1021/acsami.3c03786
ACS Appl. Mater. Interfaces 2023, 15, 24162−24174

bacteria effectively. Figure 5A and Figure S12 show that the temperature increases with glucose concentration upon laser irradiation, and a good linear correlation is obtained (y = 4.2233x + 30.363, R^2 = 0.9055) after irradiation for 5 min (Figure 5B). The results show that the TMB/Fe^{2+}/PF127/GOx hydrogel not only reaches a higher temperature when activated by glucose but also can determine the glucose concentration by monitoring the temperature change.

3.7. *In Vitro* Antibacterial Activity of the TMB/Fe^{2+}/PF127/GOx Hydrogel. Bacterial infection is one of the main factors affecting wound healing, and the antibacterial properties of the hydrogel are important to wound healing.[60] The antibacterial effects of the 2 and 10 mM of glucose-activated TMB/Fe^{2+}/PF127/GOx hydrogels are investigated under NIR irradiation. As shown in Figures 5C,D, some *S. aureus* and *E. coli* are killed by the TMB/Fe^{2+}/PF127/GOx hydrogel (group A) because of Fe^{2+}. Stronger inhibitory effects are observed from the 2 and 10 mM samples (group B and group C) without laser exposure because of the production of hydroxyl radicals from the dual catalytic processes of GOx with glucose as well as H_2O_2 with Fe^{2+}. Nevertheless, the bactericidal effects are limited because hydroxyl radicals are consumed by TMB. It is noted that *S. aureus* and *E. coli* are completely killed by the 2 or 10 mM glucose-activated TMB/Fe^{2+}/PF127/GOx hydrogel with the NIR laser. Figure 5E,F shows that the bacterial mortality rate is 100% for groups B and C with NIR, and the effectiveness is corroborated by the fluorescence staining assay (red representing dead bacteria and green representing live bacteria),[61] as shown in Figure S13.

3.8. *In Vivo* Antimicrobial Activity of the TMB/Fe^{2+}/PF127/GOx Hydrogel. Before doing the *in vivo* antimicrobial activity experiment, the cytocompatibility of the hydrogel is evaluated with NIH-3T3 cells, which are incubated with the PF127 and TMB/Fe^{2+}/PF127/GOx hydrogels. As shown in Figure S14, the cell survival rate is over 90% after 12 and 24 h, indicating low toxicity. In fact, more cells are observed after 24 than 12 h indicative of cell growth and proliferation, thereby confirming the good biocompatibility. The *in vivo* antibacterial properties are determined using a mouse model infected with *S. aureus*. The *S. aureus* solution is dropped on the wounds of the four groups: control group, positive control group, TMB/Fe^{2+}/PF127/GOx hydrogel group, and TMB/Fe^{2+}/PF127/GOx hydrogel + NIR group. The corresponding materials are coated on the wound surface, and NIR illumination is performed on the TMB/Fe^{2+}/PF127/GOx hydrogel + NIR group. The photographs taken at different times are depicted in Figure 6A. A pale yellow biofilm is observed from the control group after 3 days, but on the other hand, infection decreases for the positive control group, TMB/Fe^{2+}/PF127/GOx hydrogel group, and TMB/Fe^{2+}/PF127/GOx hydrogel + NIR group. As shown in Figures 6B,C, the wound area contracts gradually with time, and the TMB/Fe^{2+}/PF127/GOx hydrogel + NIR group shows the best regeneration results. After 12 days, the wound healing rate is 88%, which is significantly higher (P < 0.001) than that of the positive control group (57%) and control group (43%). In addition, although the wound healing rate of the TMB/Fe^{2+}/PF127/GOx hydrogel group (79%) is less than that of the TMB/Fe^{2+}/PF127/GOx hydrogel + NIR group, it is still significantly higher than that of the positive control group and control group. After 21 days, the wounds of the mice in the TMB/Fe^{2+}/PF127/GOx hydrogel + NIR group have basically healed, revealing a healing rate of 97.5%, but in contrast, some scabs and scars are observed in the hydrogel group, positive control group, and control group. The results demonstrate the synergistic effects of the TMB/Fe^{2+}/PF127/GOx hydrogel, and the PTT effect of the TMB/Fe^{2+}/PF127/GOx hydrogel kills bacteria and accelerates skin regeneration. More importantly, the blood glucose in the wound can be reduced by GOx, thereby breaking the barrier of high blood glucose to promote wound healing in the better microenvironment.[23,62] All the dressings are changed every 3 days in the healing process, and the TMB/Fe^{2+}/PF127/GOx hydrogel can be easily removed with a frozen cotton swab due to the good temperature sensitivity (refer to the video). Compared to the positive control group, wound tearing during dressing change is reduced significantly for the TMB/Fe^{2+}/PF127/GOx hydrogel.

3.9. Histological Evaluation of Regenerated Tissues. To further evaluate the quality of the regenerated tissues of the four groups, hematoxylin and eosin (H&E) staining is performed. As shown in Figure S15, the TMB/Fe^{2+}/PF127/GOx hydrogel with the desirable photothermal, hypoglycemic, and antibacterial properties mitigates the bacteria-induced inflammatory response and facilitates inflammation recovery compared to the control group, and it also exhibited a comparable therapeutic effect to the positive control (commercial hydrogel). Furthermore, more hair follicles are found from the H&E-stained wound sections of the TMB/Fe^{2+}/PF127/GOx hydrogel and TMB/Fe^{2+}/PF127/GOx hydrogel + NIR groups in comparison with the control and positive control groups. There are many hair follicles on the one treated with the TMB/Fe^{2+}/PF127/GOx hydrogel, reflecting good skin regeneration. In short, the TMB/Fe^{2+}/PF127/GOx hydrogel after NIR irradiation accelerates wound repair, promotes skin regeneration, and alleviates tissue inflammation.

Masson trichrome staining is carried out to observe collagen deposition on the tissue sections on days 10 and 21 during healing. Collagen as a basic component of healthy skin is an important indicator of the remodeling efficacy and tensile strength of damaged skin tissues. As shown in Figure 7A, the collagen content (blue region) of the four groups increases from the 10th to 21st days. In particular, the collagen content of the TMB/Fe^{2+}/PF127/GOx hydrogel + NIR group is larger than that of the control group (P < 0.01), positive control, and TMB/Fe^{2+}/PF127/GOx hydrogel group (P < 0.05), demonstrating that collagen deposition in granulation tissues is fostered by the TMB/Fe^{2+}/PF127/GOx hydrogel in conjunction with the photothermal effect (Figure 7C).

To further evaluate the physiological mechanism of wound healing, immunofluorescence staining of some cytokines is carried out. During wound healing, changes of cytokines such as interleukin-6 (IL-6), vascular endothelial growth factor (VEGF), and matrix metalloproteinase-2 (MMP-2) are related to cell metabolism and proliferation. The IL-6 expression has a positive correlation with the degree of inflammation, and VEGF has an important proangiogenic function in the proliferative phase of diabetic wound healing, so it can be used to evaluate the formation of neovascularization. MMP-2 has been shown to play an important role in wound healing, but it is inhibited in a high glucose concentration environment. As shown in Figure 7B, the nuclei stained with DAPI are shown in blue, whereas IL-6, VEGF, and MMP-2 are shown in green. It can be observed that the expression levels of IL-6 in the TMB/Fe^{2+}/PF127/GOx hydrogel and TMB/Fe^{2+}/PF127/

https://doi.org/10.1021/acsami.3c03786
ACS Appl. Mater. Interfaces 2023, 15, 24162−24174

GOx hydrogel + NIR group are lower than those of the control group, and there is an obvious difference with $P < 0.01$ (Figure 7D), which effectively alleviates the inflammatory reaction due to the good photothermal antibacterial ability and local hypoglycemic ability of the hydrogel, which are consistent with H&E staining. On the other hand, the expression levels of VEGF and MMP-2 of the TMB/Fe^{2+}/PF127/GOx hydrogel + NIR group are higher than those of the other three groups on account of the synergistic bactericidal action of the hydrogel and thermal sterilization (Figures 7E,F). Therefore, by downregulating the expression of IL-6 and upregulating those of VEGF and MMP-2, the TMB/Fe^{2+}/PF127/GOx hydrogel delivers excellent healing performance.[26]

3.10. *In Vivo* Safety Evaluation. Safety evaluation is necessary for clinical adoption, so the biocompatibility of the TMB/Fe^{2+}/PF127/GOx hydrogel is evaluated by histological analysis, hemanalysis, and biochemical analysis. As shown in Figure S16, no obvious damage, inflammatory lesions, or abnormalities are observed from the major organs of the positive control group, TMB/Fe^{2+}/PF127/GOx hydrogel group, and TMB/Fe^{2+}/PF127/GOx hydrogel + NIR group 21 days after the treatment. Furthermore, the weight of the mice increases continuously, suggesting normal growth (Figure S17). Blood is collected from the mice for biochemical assessment, and all the indexes show no abnormalities. The concentrations of white blood cells and neutrophils are significantly lower than those of the control group (Figure S18). Therefore, inflammation is mitigated and there is an adverse reaction, indicating that the TMB/Fe^{2+}/PF127/GOx hydrogel has high biosafety in wound healing of diabetic patients.

4. CONCLUSIONS

The injectable, self-reparable, and on-demand removable TMB/Fe^{2+}/PF127/GOx hydrogel dressing with blood glucose monitoring, hypoglycemia effects, good biocompatibility, and excellent PTT/CDT antibacterial activity is designed and fabricated to accelerate the healing of bacteria-infected skin wounds for diabetic patients. The hydrogel with good fluidity and temperature sensitivity adheres firmly to wounds *in vivo*, thereby avoiding hydrogel shedding from the wound in spite of mechanical movement. The local glucose concentration in the vicinity of the wound decreases because of continuous consumption of glucose by GOx to facilitate wound healing. It is demonstrated that glucose can further activate the generation of oxidized TMB to produce excellent photothermal/chemodynamic antibacterial effects to reduce bacterial infection and accelerate wound healing. The TMB/Fe^{2+}/PF127/GOx hydrogel not only is suitable for the regulation and monitoring of glucose concentration in diabetic wounds but also can prevent bacterial infections photothermally/chemodynamically and promote wound healing by adjusting the important cytokines. The materials and strategy reported in this paper have great potential in the clinical treatment of wounds for diabetic patients.

ASSOCIATED CONTENT

Supporting Information

The Supporting Information is available free of charge at https://pubs.acs.org/doi/10.1021/acsami.3c03786.

Video showing treatment with and removal of the hydrogel (MP4)

UV−vis spectrum; actual pictures of the hydrogel; photothermal pictures; confocal fluorescence images; H&E staining images; and biochemical analysis (PDF)

AUTHOR INFORMATION

Corresponding Authors

Ai-Guo Shen − *College of Chemistry and Chemical Engineering, Wuhan Textile University, Wuhan 430200, P.R. China*; orcid.org/0000-0002-3762-1703; Email: agshen@whu.edu.cn

Paul K. Chu − *Department of Physics, Department of Materials Science and Engineering, and Department of Biomedical Engineering, City University of Hong Kong, Hong Kong 999077, P.R. China*; orcid.org/0000-0002-5581-4883; Email: paul.chu@cityu.edu.hk

Authors

Wei Zhu − *College of Chemistry and Chemical Engineering, Wuhan Textile University, Wuhan 430200, P.R. China*

Ya-Qin Liu − *College of Chemistry and Chemical Engineering, Wuhan Textile University, Wuhan 430200, P.R. China*

Pei Liu − *Department of Physics, Department of Materials Science and Engineering, and Department of Biomedical Engineering, City University of Hong Kong, Hong Kong 999077, P.R. China*

Jun Cao − *College of Chemistry and Chemical Engineering, Wuhan Textile University, Wuhan 430200, P.R. China*

Complete contact information is available at: https://pubs.acs.org/10.1021/acsami.3c03786

Author Contributions

[$]W.Z. and Y.-Q.L. contributed equally to this paper.

Author Contributions

The manuscript was written through contributions of all authors. All authors have given approval to the final version of the manuscript.

Funding

National Natural Science Foundation of China (Nos. 21874102, 21775114, and 22074109), China Postdoctoral Science Foundation (2021 M702506), City University of Hong Kong Donation Research Grant (DON-RMG No. 9229021), City University of Hong Kong Strategic Research Grant (SRG No. 7005505), City University of Hong Kong Donation Grant (No. 9220061), Hong Kong PDFS-RGC Postdoctoral Fellowship Scheme (PDFS2122-1S08 and CityU 9061014), as well as Hong Kong HMRF (Health and Medical Research Fund) (2120972 and CityU 9211320)

Notes

The authors declare no competing financial interest.

ACKNOWLEDGMENTS

We thank Dr. Xiao-Dong Zhou and Dr. Xin-Yi Li from the Core Facility of Wuhan University for assistance in the UV−vis and FE-SEM analysis.

REFERENCES

(1) Rodrigues, M.; Kosaric, N.; Bonham, C. A.; Gurtner, G. C. Wound Healing: A Cellular Perspective. *Physiol. Rev.* **2019**, *99*, 665−706.

(2) Misra, A.; Gopalan, H.; Jayawardena, R.; Hills, A. P.; Soares, M.; Reza-Albarrán, A. A.; Ramaiya, K. L. Diabetes in Developing Countries. *J. Diabetes* **2019**, *11*, 522−539.

(3) Sun, H.; Saeedi, P.; Karuranga, S.; Pinkepank, M.; Ogurtsova, K.; Duncan, B. B.; Stein, C.; Basit, A.; Chan, J. C. N.; Mbanya, J. C.; Pavkov, M. E.; Ramachandaran, A.; Wild, S. H.; James, S.; Herman, W. H.; Zhang, P.; Bommer, C.; Kuo, S.; Boyko, E. J.; Magliano, D. J. IDF Diabetes Atlas: Global, Regional and Country-level Diabetes Prevalence Estimates for 2021 and Projections for 2045. *Diabetes Res. Clin. Pract.* **2022**, No. 109119.
(4) Gurtner, G. C.; Werner, S.; Barrandon, Y.; Longaker, M. T. Wound Repair and Regeneration. *Nature* **2008**, *453*, 314−321.
(5) American Diabetes Association. Introduction: Standards of Medical Care in Diabetes-2022. *Diabetes Care* **2022**, *45*, S1−S2.
(6) Jeffcoate, W. J.; Vileikyte, L.; Boyko, E. J.; Armstrong, D. G.; Boulton, A. J. Current Challenges and Opportunities in the Prevention and Management of Diabetic Foot Ulcers. *Diabetes Care* **2018**, *41*, 645−652.
(7) Liang, Y.; Li, M.; Yang, Y.; Qiao, L.; Xu, H.; Guo, B. pH/Glucose Dual Responsive Metformin Release Hydrogel Dressings with Adhesion and Self-Healing via Dual-Dynamic Bonding for Athletic Diabetic Foot Wound Healing. *ACS Nano* **2022**, *16*, 3194−3207.
(8) Shaikh-Kader, A.; Houreld, N. N.; Rajendran, N. K.; Abrahamse, H. The Link between Advanced Glycation End Products and Apoptosis in Delayed Wound Healing. *Cell Biochem. Funct.* **2019**, *37*, 432−442.
(9) Okamoto, T.; Yamagishi, S.; Inagaki, Y.; Amano, S.; Koga, K.; Abe, R.; Takeuchi, M.; Ohno, S.; Yoshimura, A.; Makita, Z. Angiogenesis Induced by Advanced Glycation End Products and Its Prevention by cerivastatin. *FASEB J.* **2002**, *16*, 1928−1930.
(10) Yaseen, H.; Khamaisi, M. Skin Well-being in Diabetes: Role of Macrophages. *Cell. Immunol.* **2020**, *356*, No. 104154.
(11) Powers, J. G.; Higham, C. K.; Broussard, T.; Phillips, J. Wound Healing and Treating Wounds: Chronic Wound Care and Management. *J. Am. Acad. Dermatol.* **2016**, *74*, 607−625.
(12) Moura, L. I. F.; Dias, A. M. A.; Carvalho, E.; de Sousa, H. C. Recent Advances on the Development of Wound Dressings for Diabetic Foot Ulcer Treatment—A Review. *Acta Biomater.* **2013**, *9*, 7093−7114.
(13) Han, G.; Ceilley, R. Chronic Wound Healing: A Review of Current Management and Treatments. *Adv. Ther.* **2017**, *34*, 599−610.
(14) Farahani, M.; Shafiee, A. Wound Healing: From Passive to Smart Dressings. *Adv. Healthcare Mater.* **2021**, *10*, 2100477.
(15) Abou-Okeil, A.; Fahmy, H. M.; El-Bisi, M. K.; Ahmed-Farid, O. A. Hyaluronic Acid/Na-alginate Films as Topical Bioactive Wound Dressings. *Eur. Polym. J.* **2018**, *109*, 101−109.
(16) Kim, S.; Park, S. G.; Kang, S. W.; Lee, K. J. Nanofiber-Based Hydrocolloid from Colloid Electrospinning Toward Next Generation Wound Dressing. *Macromol. Mater. Eng.* **2016**, *301*, 818−826.
(17) Dong, R.; Guo, B. Smart Wound Dressings for Wound Healing. *Nano Today* **2021**, *41*, No. 101290.
(18) Liang, Y.; He, J.; Guo, B. Functional Hydrogels as Wound Dressing to Enhance Wound Healing. *ACS Nano* **2021**, *15*, 12687−12722.
(19) Maleki, A.; He, J. H.; Bochani, S.; Nosrati, V.; Shahbazi, M. A.; Guo, B. L. Multifunctional Photoactive Hydrogels for Wound Healing Acceleration. *ACS Nano* **2021**, *15*, 18895−18930.
(20) Ghobril, C.; Grinstaff, M. W. The Chemistry and Engineering of Polymeric Hydrogel Adhesives for Wound Closure: a Tutorial. *Chem. Soc. Rev.* **2015**, *44*, 1820−1835.
(21) Griffin, D. R.; Weaver, W. M.; Scumpia, P. O.; Carlo, D. D.; Segura, T. Accelerated Wound Healing by Injectable Microporous Gel Scaffolds Assembled From Annealed Building Blocks. *Nat. Mater.* **2015**, *14*, 737−744.
(22) Jiang, Y.; Zhang, X.; Zhang, W.; Wang, M.; Yan, L.; Wang, K.; Han, L.; Lu, X. Infant Skin Friendly Adhesive Hydrogel Patch Activated at Body Temperature for Bioelectronics Securing and Diabetic Wound Healing. *ACS Nano* **2022**, *16*, 8662−8676.
(23) Zhou, W.; Duan, Z.; Zhao, J.; Fu, Z.; Zhu, C.; Fan, D. Glucose and MMP-9 Dual-Responsive Hydrogel with Temperature Sensitive Self-adaptive Shape and Controlled Drug Release Accelerates Diabetic Wound Healing. *Bioact. Mater.* **2022**, *17*, 1−17.
(24) Zhu, J.; Zhou, H.; Gerhard, E. M.; Zhang, S.; Rodríguez, F. I. P.; Pan, T.; Yang, H.; Lin, Y.; Yang, J.; Cheng, H. Smart Bioadhesives for Wound Healing and Closure. *Bioact. Mater.* **2023**, *19*, 360−375.
(25) Guo, Z.; Zhang, Z.; Zhang, N.; Gao, W.; Li, J.; Pu, Y.; He, B.; Xie, J. A Mg^{2+}/Polydopamine Composite Hydrogel for the Acceleration of Infected Wound Healing. *Bioact. Mater.* **2022**, *9*, 203−221.
(26) Shao, Z.; Yin, T.; Jiang, J.; He, Y.; Xiang, T.; Zhou, S. Wound Microenvironment Self-Adaptive Hydrogel with Efficient Angiogenesis for Promoting Diabetic Wound Healing. *Bioact. Mater.* **2023**, *20*, 561−573.
(27) Sun, X.; Jia, P.; Zhang, H.; Dong, M.; Wang, J.; Li, L.; Bu, T.; Wang, X.; Wang, L.; Lu, Q.; Wang, J. Green Regenerative Hydrogel Wound Dressing Functionalized by Natural Drug-Food Homologous Small Molecule Self-Assembled Nanospheres. *Adv. Funct. Mater.* **2022**, *32*, 2106572.
(28) Chen, R.; Zhao, C.; Chen, Z.; Shi, X.; Zhu, H.; Bu, Q.; Wang, L.; Wang, C.; He, H. A Bionic Cellulose Nanofiber-based Nanocage Wound Dressing for NIR-Triggered Multiple Synergistic Therapy of Tumors and Infected Wounds. *Biomaterials* **2022**, *281*, 121330−121342.
(29) Zeng, Q.; Qi, X.; Shi, G.; Zhang, M.; Haick, H. Wound Dressing: From Nanomaterials to Diagnostic Dressings and Healing Evaluations. *ACS Nano* **2022**, *16*, 1708−1733.
(30) Yin, M.; Wu, J.; Deng, M.; Wang, P.; Ji, G.; Wang, M.; Zhou, C.; Blum, N.; Zhang, W.; Shi, H.; Jia, N.; Wang, X.; Huang, P. Multifunctional Magnesium Organic Framework-Based Microneedle Patch for Accelerating Diabetic Wound Healing. *ACS Nano* **2021**, *15*, 17842−17853.
(31) Pang, Q.; Lou, D.; Li, S.; Wang, G.; Qiao, B.; Dong, S.; Ma, L.; Gao, C.; Wu, Z. Smart Flexible Electronics-Integrated Wound Dressing for Real-Time Monitoring and On-Demand Treatment of Infected Wounds. *Adv. Sci.* **2020**, *7*, 1902673.
(32) Li, Y.; Wang, D.; Wen, J.; Yu, P.; Liu, J.; Li, J.; Chu, H. Chemically Grafted Nanozyme Composite Cryogels to Enhance Antibacterial and Biocompatible Performance for Bioliquid Regulation and Adaptive Bacteria Trapping. *ACS Nano* **2021**, *15*, 19672−19683.
(33) Mao, C.; Xiang, Y.; Liu, X.; Cui, Z.; Yang, X.; Yeung, K. W. K.; Pan, H.; Wang, X.; Chu, P. K.; Wu, S. Photo-Inspired Antibacterial Activity and Wound Healing Acceleration by Hydrogel Embedded with Ag/Ag@AgCl/ZnO Nanostructures. *ACS Nano* **2017**, *11*, 9010−9021.
(34) Wang, Y.; Zhao, Y. N.; Wu, J. L.; Tan, J.; Fu, W. S.; Tang, H.; Zhang, P. Negatively Charged Sulfur Quantum Dots for Treatment of Drug-Resistant Pathogenic Bacterial Infections. *Nano Lett.* **2021**, *21*, 9433−9441.
(35) Li, Y.; Liu, X.; Cui, Z.; Zheng, Y.; Jiang, H.; Zhang, Y.; Liang, Y.; Li, Z.; Zhu, S.; Wu, S. Treating Multi-Drug-Resistant Bacterial Infections by Functionalized Nano-Bismuth Sulfide through the Synergy of Immunotherapy and Bacteria-Sensitive Phototherapy. *ACS Nano* **2022**, *16*, 14860−14873.
(36) Darvishi, S.; Tavakoli, S.; Kharaziha, M.; Girault, H. H.; Kaminski, C. F.; Mela, I. Advances in the Sensing and Treatment of Wound Biofilms. *Angew. Chem., Int. Ed.* **2022**, *61*, 202112218.
(37) Duan, S.; Wu, R.; Xiong, Y. H.; Ren, H. M.; Lei, C.; Zhao, Y. Q.; Zhang, X. Y.; Xu, F. J. Multifunctional Antimicrobial Materials: From Rational Design to Biomedical Applications. *Prog. Mater. Sci.* **2022**, *125*, 100887−100932.
(38) Thompson, S. A.; Paterson, S.; Azab, M. M. M.; Wark, A. W.; Rica, R. Light-Triggered Inactivation of Enzymes with Photothermal Nanoheaters. *Small* **2017**, *13*, 1603195.
(39) Wang, T.; Dong, D.; Chen, T.; Zhu, J.; Wang, S.; Wen, W.; Zhang, X.; Tang, H.; Liang, J.; Wang, S.; Xiong, H. Acidity-Responsive Cascade Nanoreactor based on Metal-Nanozyme and Glucose Oxidase Combination for Starving and Photothermal-

https://doi.org/10.1021/acsami.3c03786
ACS Appl. Mater. Interfaces 2023, 15, 24162−24174

Enhanced Chemodynamic Antibacterial Therapy. *Chem. Eng. J.* **2022**, *446*, No. 137172.
(40) Lu, W.; Guo, Y.; Zhang, J.; Yue, Y.; Fan, L.; Li, F.; Dong, C.; Shuang, S. A High Catalytic Activity Nanozyme Based on Cobalt-Doped Carbon Dots for Biosensor and Anticancer Cell Effect. *ACS Appl. Mater. Interfaces* **2022**, *14*, 57206−57214.
(41) Zhu, J.; He, G.; Chen, P. H.; Zhang, Y.; Zhang, Y.; Lei, S.; Zhang, Y.; Li, M.; Huang, P.; Lin, J. Terpyridine-Grafted Nitrogen-Terminal Endowing Cyanine with Metal-Ion-Regulated Photophysical Properties for Cancer Theranostics. *Research* **2023**, *6*, 61.
(42) Zhang, X.; Lin, S.; Zhao, F.; Zhang, J.; Lei, S.; Bai, F.; Liu, Q.; Wu, J.; He, T.; Huang, P.; Lin, J. Programmably Controllable Delivery of Metastable Ferrous Ions for Multiscale Dynamic Imaging Guided Photothermal Primed Chemodynamic Therapy. *Adv. Mater.* **2023**, 2210876.
(43) He, T.; Jiang, C.; He, J.; Zhang, Y.; He, G.; Wu, J.; Lin, J.; Zhou, X.; Huang, P. Manganese-Dioxide-Coating-Instructed Plasmonic Modulation of Gold Nanorods for Activatable Duplex-Imaging-Guided NIR-II Photothermal-Chemodynamic Therapy. *Adv. Mater.* **2021**, *33*, 2008540.
(44) He, T.; Yuan, Y.; Jiang, C.; Blum, N. T.; He, J.; Huang, P.; Lin, J. Light-Triggered Transformable Ferrous Ion Delivery System for Photothermal Primed Chemodynamic Therapy. *Angew. Chem., Int. Ed.* **2021**, *60*, 6047−6054.
(45) Yang, C.; Younis, M. R.; Zhang, J.; Qu, J.; Lin, J.; Huang, P. Programmable NIR-II Photothermal-Enhanced Starvation-Primed Chemodynamic Therapy using Glucose Oxidase-Functionalized Ancient Pigment Nanosheets. *Small* **2020**, *16*, 2001518.
(46) He, R. Y.; Liu, H.; Fang, T. S.; Niu, Y.; Zhang, H. Q.; Han, F.; Gao, B.; Li, F.; Xu, F. A Colorimetric Dermal Tattoo Biosensor Fabricated by Microneedle Patch for Multiplexed Detection of Health-related Biomarkers. *Adv. Sci.* **2021**, *8*, 2103030.
(47) Zhang, P.; Sun, D.; Cho, A.; Weon, S.; Lee, S.; Lee, J.; Han, J. W.; Kim, D. P.; Choi, W. Modified Carbon Nitride Nanozyme as Bifunctional Glucose Oxidase-Peroxidase for Metal-Free Bioinspired Cascade Photocatalysis. *Nat. Commun.* **2019**, *10*, 940−953.
(48) Ma, Z.; Foda, M. F.; Liang, H.; Zhao, Y.; Han, H. In Situ Nanozyme-Amplified NIR-II Phototheranostics for Tumor-Specific Imaging and Therapy. *Adv. Funct. Mater.* **2021**, *31*, 2103765.
(49) Yang, Y.; Wang, J. C.; Zhang, X.; Lu, W. L.; Zhang, Q. A Novel Mixed Micelle Gel with Thermo-Sensitive Property for the Local Delivery of Docetaxel. *J. Controlled Release* **2009**, *135*, 175−182.
(50) Liu, Z.; Tang, W.; Liu, J.; Han, Y.; Yan, Q.; Dong, Y.; Liu, X.; Yang, D.; Ma, G.; Cao, H. A Novel Sprayable Thermosensitive Hydrogel Coupled with Zinc Modified Metformin Promotes the Healing of Skin Wound. *Bioact. Mater.* **2023**, *20*, 610−626.
(51) Zhang, J.; Wang, L.; Lei, J.; Liu, Y.; Zhang, J. Photo-Fenton Degradation of Phenol by CdS/rGO/Fe^{2+} at Natural pH with In Situ-Generated H_2O_2. *Appl. Catal., B* **2019**, *241*, 367−374.
(52) Pu, Y.; Wu, W.; Zhou, B.; Xiang, H.; Yu, J.; Yin, H.; Zhang, Y.; Du, D.; Chen, Y.; Xu, H. Starvation Therapy Enabled "switch-on" NIR-II Photothermal Nanoagent for Synergistic in situ Photothermal Immunotherapy. *Nano Today* **2022**, *44*, No. 101461.
(53) Zhou, S.; Guo, K.; Bukhvalov, D.; Zhang, X. F.; Zhu, W.; Yao, J.; He, M. Cellulose Hydrogels by Reversible Ion-Exchange as Flexible Pressure Sensors. *Adv. Mater. Technol.* **2020**, *5*, 2000358.
(54) Tang, X.; Wang, X.; Sun, Y.; Zhao, L.; Li, D.; Zhang, J.; Sun, H.; Yang, B. Magnesium Oxide-Assisted Dual-Cross-Linking Bio-Multifunctional Hydrogels for Wound Repair during Full Thickness Skin Injuries. *Adv. Funct. Mater.* **2021**, *31*, 2105718.
(55) Jin, S.; Kim, S.; Kim, D. S.; Son, D.; Shin, M. Optically Anisotropic Topical Hemostatic Coacervate for Naked-Eye Identification of Blood Coagulation. *Adv. Funct. Mater.* **2022**, *32*, 211032.
(56) Fu, L. H.; Qi, C.; Lin, J.; Huang, P. Catalytic Chemistry of Glucose Oxidase in Cancer Diagnosis and Treatment. *Chem. Soc. Rev.* **2018**, *47*, 6454−6472.
(57) Fu, L. H.; Qi, C.; Hu, Y. R.; Lin, J.; Huang, P. Glucose Oxidase-Instructed Multimodal Synergistic Cancer Therapy. *Adv. Mater.* **2019**, *31*, 1808325.
(58) Zhang, Y.; Wan, Y.; Liao, Y.; Hu, Y.; Jiang, T.; He, T.; Bi, W.; Lin, J.; Gong, P.; Tang, L.; Huang, P. Janusγ-Fe_2O_3/SiO_2-Based Nanotheranostics for Dual-Modal Imaging and Enhanced Synergistic Cancer Starvation/Chemodynamic Therapy. *Sci. Bull.* **2020**, *65*, 564−572.
(59) Du, S.; Suo, H.; Xie, G.; Lyu, Q.; Mo, M.; Xie, Z.; Zhou, N.; Zhang, L.; Tao, J.; Zhu, J. Self-Powered and Photothermal Electronic Skin Patches for Accelerating Wound Healing. *Nano Energy* **2022**, *93*, No. 106906.
(60) Zheng, S.; Li, W.; Ren, Y.; Liu, Z.; Zou, X.; Hu, Y.; Guo, J.; Sun, Z.; Yan, F. Moisture-Wicking, Breathable, and Intrinsically Antibacterial Electronic Skin Based on Dual-Gradient Poly(ionic liquid) Nanofiber Membranes. *Adv. Mater.* **2021**, *34*, 2106570.
(61) Zhu, W.; Zhang, L.; Yang, Z.; Liu, P.; Wang, J.; Cao, J.; Shen, A.; Xu, Z.; Wang, J. An Efficient Tumor-Inducible Nanotheranostics for Magnetic Resonance Imaging and Enhanced Photodynamic Therapy. *Chem. Eng. J.* **2019**, *358*, 969−979.
(62) Liu, X.; Yan, Z.; Zhang, Y.; Liu, Z.; Sun, Y.; Ren, J.; Qu, X. Two-Dimensional Metal-Organic Framework/Enzyme Hybrid Nanocatalyst as a Benign and Self-Activated Cascade Reagent for in Vivo Wound Healing. *ACS Nano* **2019**, *13*, 5222−5230.

https://doi.org/10.1021/acsami.3c03786
ACS Appl. Mater. Interfaces 2023, 15, 24162−24174

Supporting Information

Blood Glucose-Depleting Hydrogel Dressing as Activatable Photothermal/Chemodynamic Antibacterial Agent for Healing Diabetic Wounds

Wei Zhu [†,$], *Ya-Qin Liu* [†,$], *Pei Liu* [‡], *Jun Cao* [†], *Ai-Guo Shen* [†,*], *Paul K. Chu* [‡,*]

[†] College of Chemistry and Chemical Engineering, Wuhan Textile University, Wuhan 430200, P. R. China

[‡] Department of Physics, Department of Materials Science and Engineering, and Department of Biomedical Engineering, City University of Hong Kong, Tat Chee Avenue, Kowloon, Hong Kong 999077, P. R. China

[$] W.Z. and Y.L. contributed equally to this paper

[*] Corresponding authors: Prof. Dr. Ai-Guo Shen, E-mail: agshen@whu.edu.cn; Prof. Dr. Paul K. Chu, E-mail: paul.chu@cityu.edu.hk.

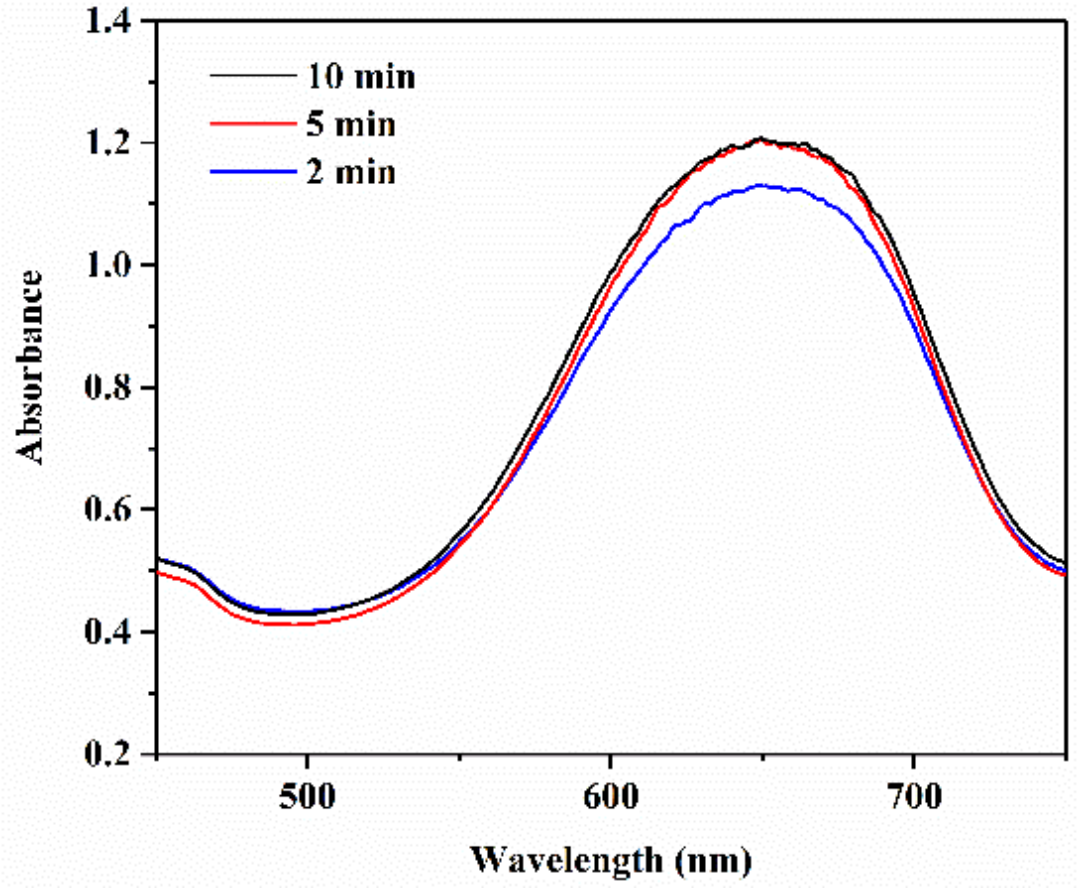

Figure S1. Reaction time optimization of the TMB/Fe^{2+}/PF127 hydrogel with H_2O_2 with an Fe^{2+} concentration of 1 mg/mL.

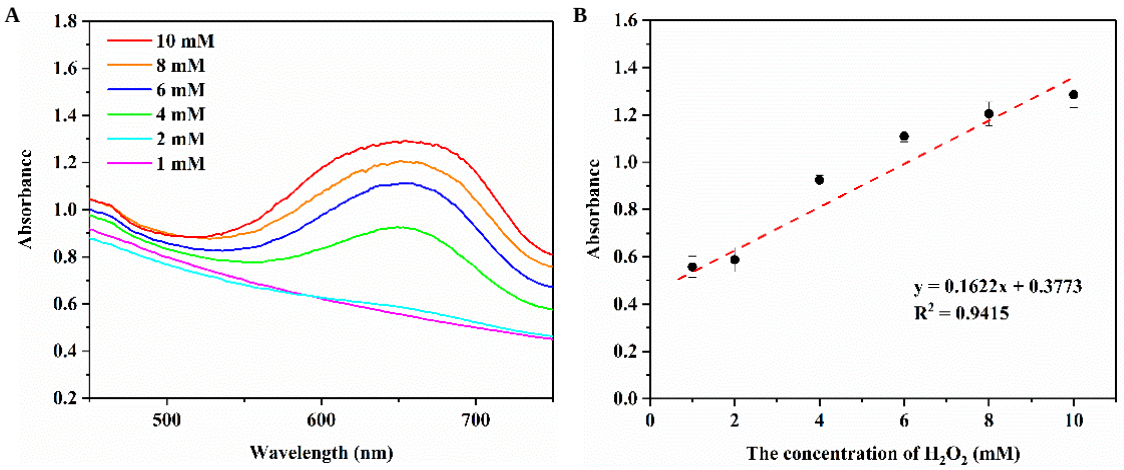

Figure S2. (A) UV-vis spectra of the products after the reaction in H_2O_2 solutions with different concentrations and TMB/Fe^{2+}/PF127 hydrogel and (B) Calibration curve of the H_2O_2 concentration versus absorbance at 652 nm. The error bars represent the standard deviations of three independent experiments.

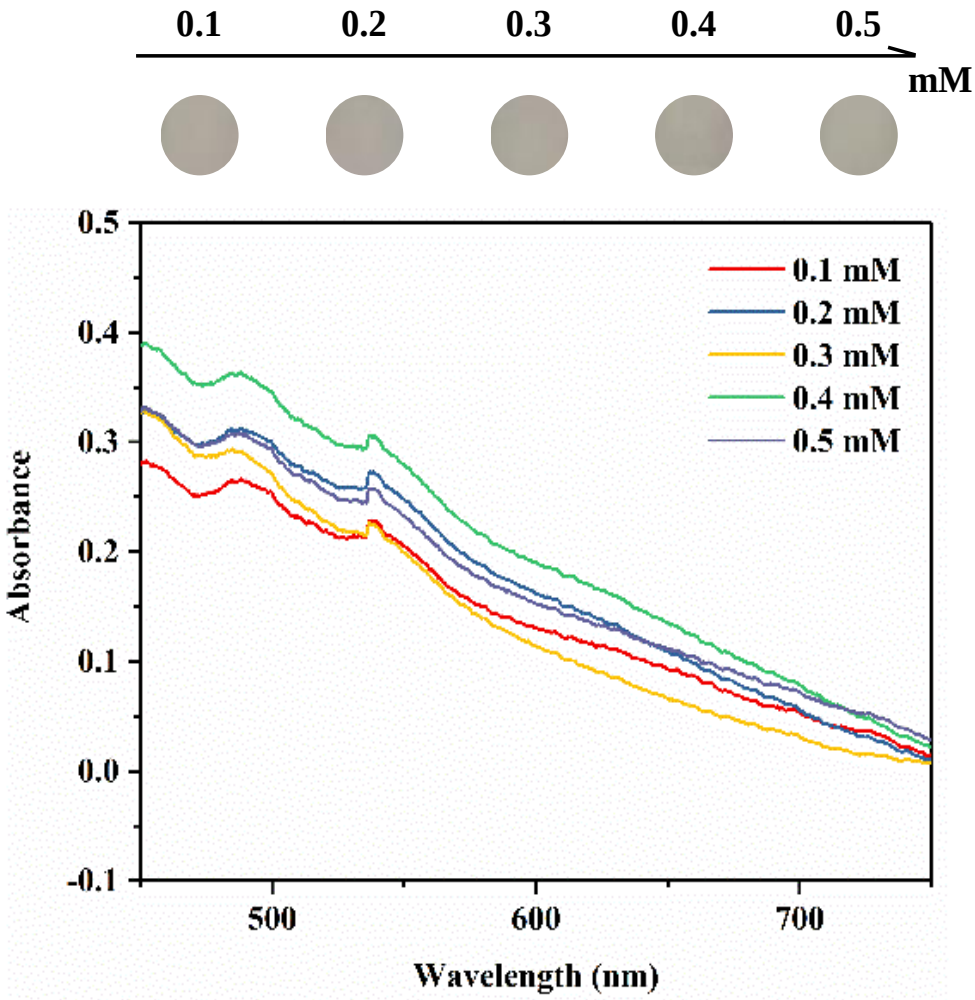

Figure S3. Pictures of the products after the reaction in the solutions with different H_2O_2 concentrations from 0.1 to 0.5 mM and TMB/Fe^{2+}/PF127 hydrogel together with the UV-vis spectra of the products.

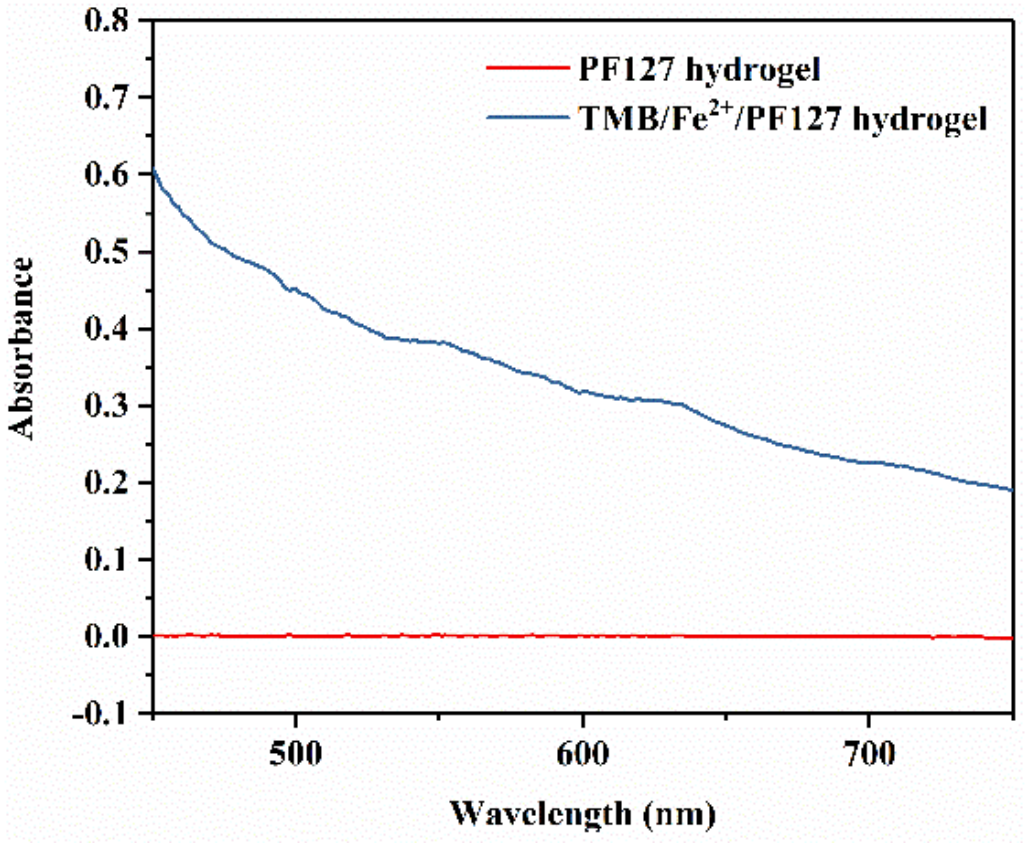

Figure S4. UV-vis absorption spectra of the PF127 hydrogel and TMB/Fe^{2+}/PF127 hydrogel.

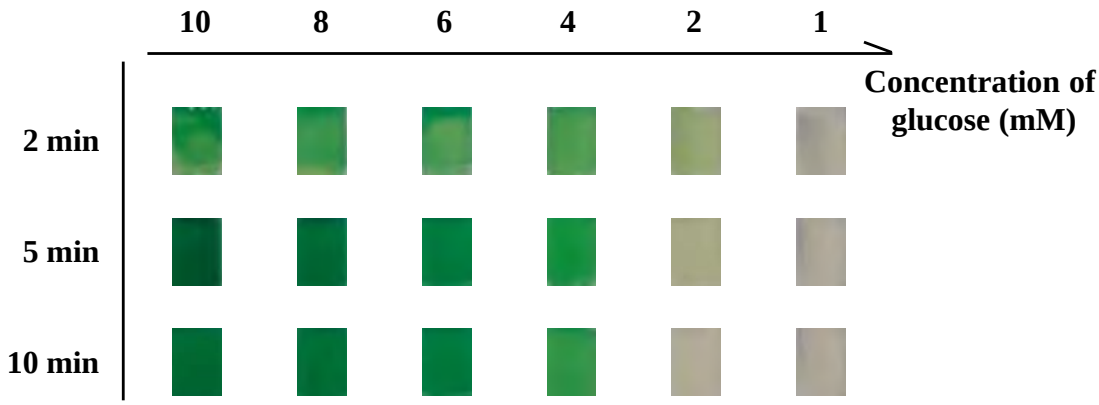

Figure S5. Optimization of reaction time for glucose detection of the TMB/Fe^{2+}/PF127/GOx hydrogel.

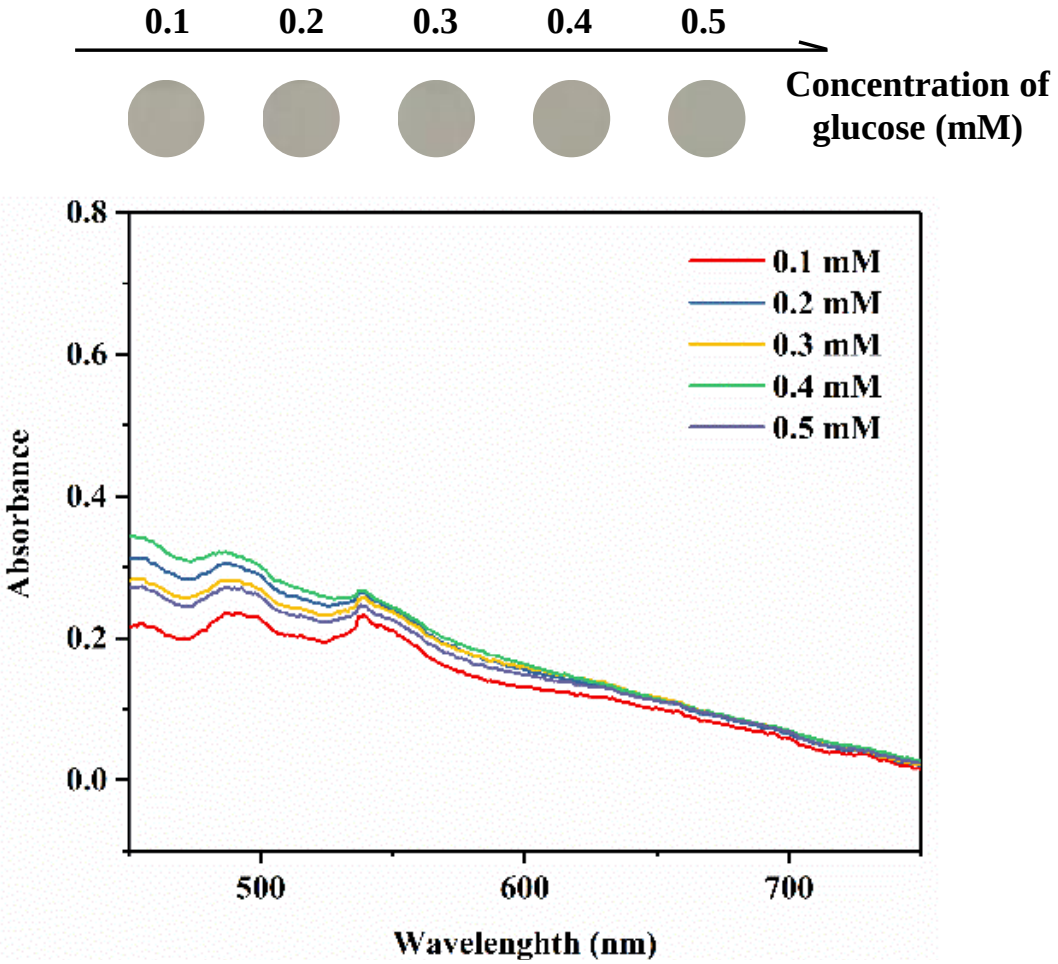

Figure S6. Pictures of the products after the reaction in solutions with different glucose concentrations from 0.1 to 0.5 mM and TMB/Fe^{2+}/PF127 hydrogel together with the UV-vis spectra of the products.

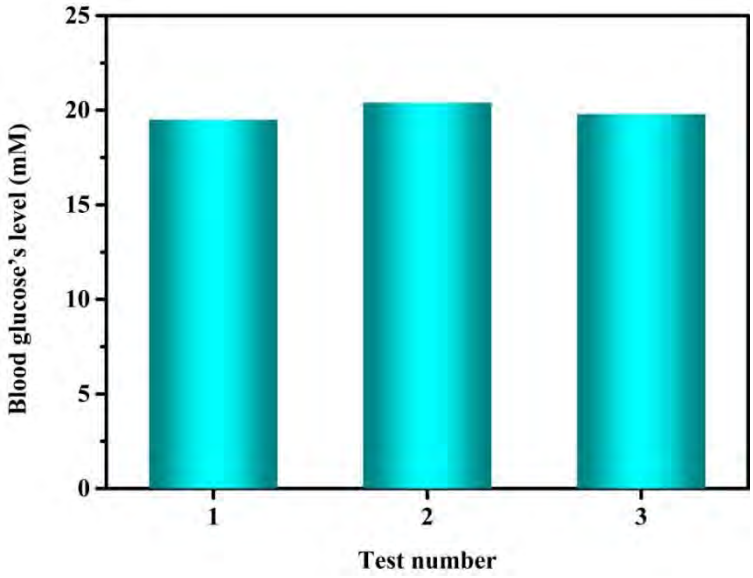

Figure S7. Actual blood glucose's level of db/db mouse with three test.

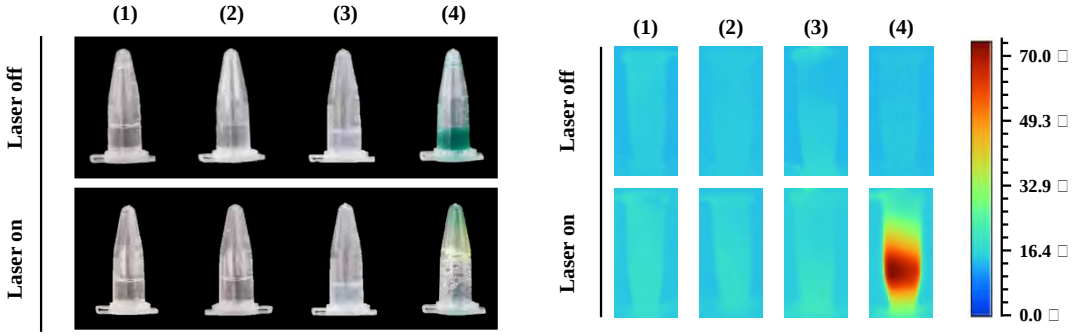

(1) Control (2) PF127 hydrogel (3) TMB/Fe^{2+}/PF127/GOx hydrogel

(4) TMB/Fe^{2+}/PF127/GOx hydrogel+ 10 mM of Glucose

Figure S8. Photothermal properties of the glucose-triggered TMB/Fe^{2+}/PF127 hydrogel: (A) Photographs of the samples before and after laser irradiation and (B) Infrared images before and after laser irradiation.

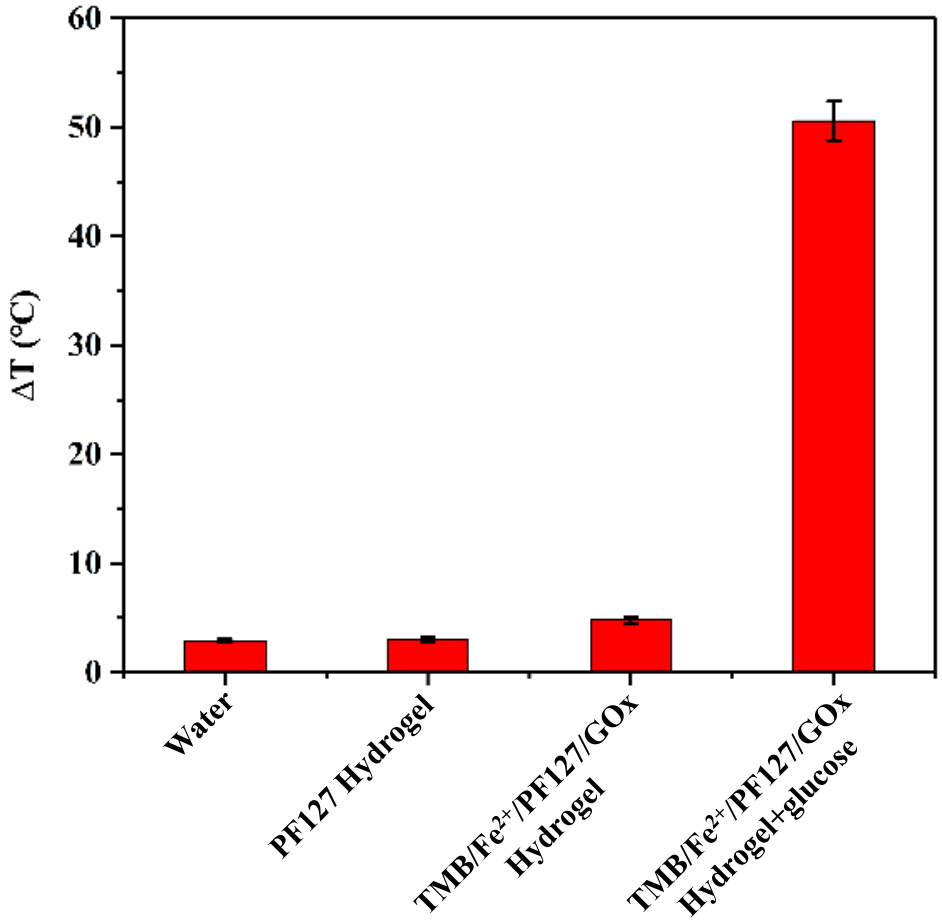

Figure S9. Temperature changes of the control group, PF127 hydrogel group, TMB/Fe^{2+}/PF127/GOx hydrogel group, and glucose-triggered TMB/Fe^{2+}/PF127/GOx hydrogel group before and after irradiation. The error bars are derived from the standard deviations of three independent experiments.

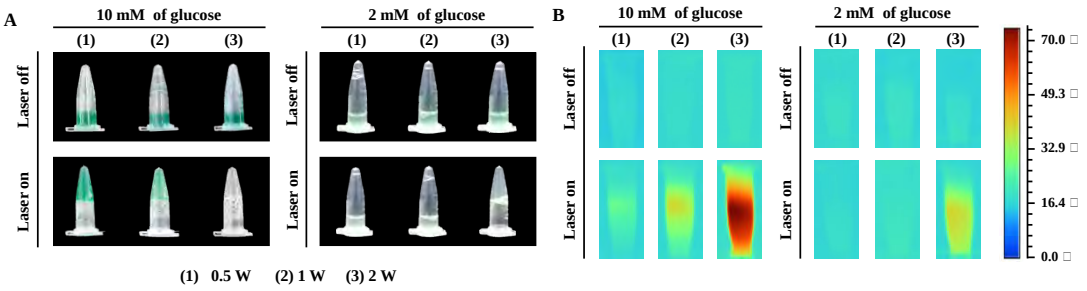

Figure S10. Laser power optimization: (A) Pictures of the TMB/Fe^{2+}/PF127/GOx hydrogel in the 2 mM or 10 mM glucose solution before and after laser irradiation with different power and (B) Infrared images of the TMB/Fe^{2+}/PF127/GOx hydrogel in the 2 mM or 10 mM glucose solution before and after laser irradiation with different power.

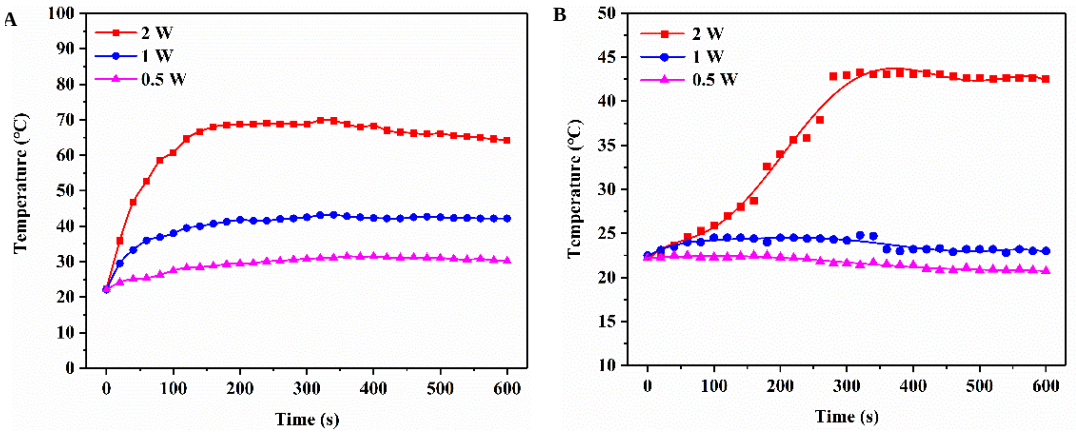

Figure S11. Temperature change with time of the TMB/Fe^{2+}/PF127/GOx hydrogel upon laser irradiation with different power: (A) 10 mM glucose solution and (B) 2 mM glucose solution.

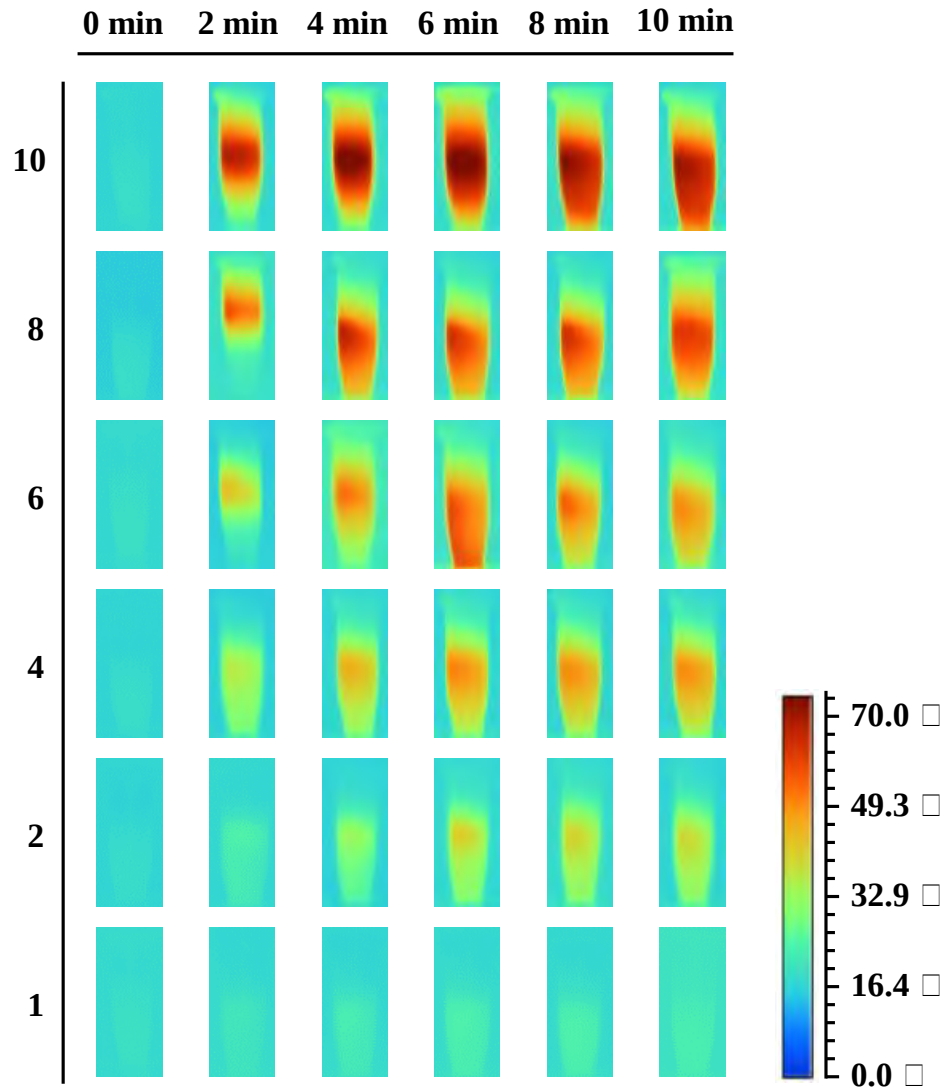

Figure S12. Infrared images of the TMB/Fe^{2+}/PF127/GOx hydrogel in solutions with different glucose concentrations upon 2 W laser illumination.

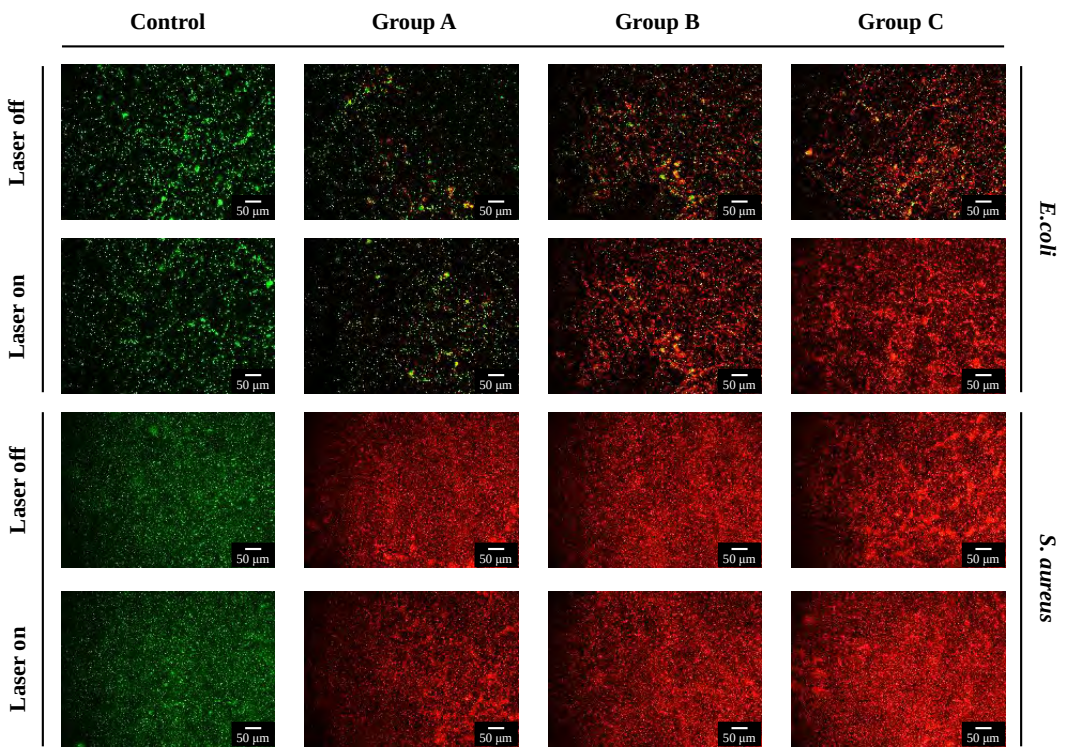

Figure S13. Confocal fluorescence staining of the bacteria of different groups before and after laser exposure.

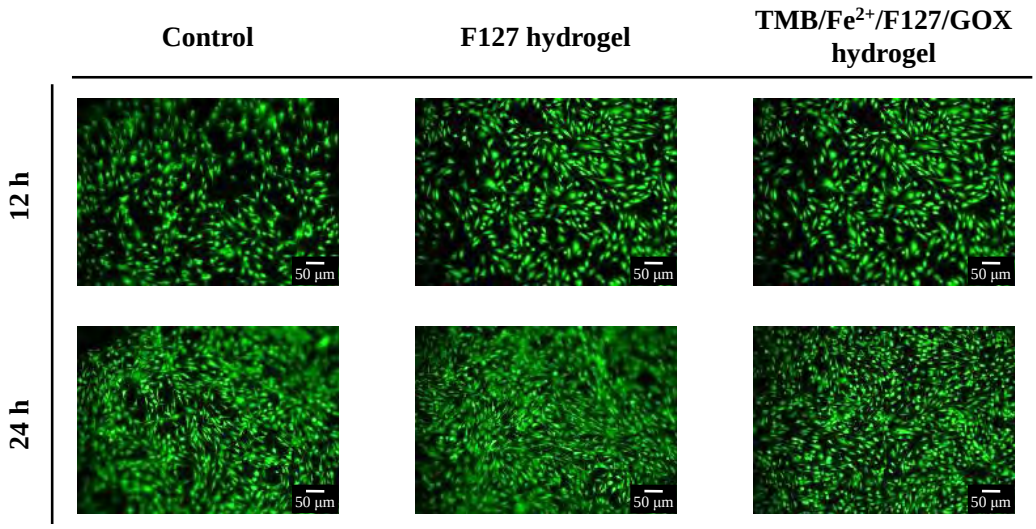

Figure S14. Confocal fluorescence images of NIH-3T3 cells incubated with the F127 hydrogel and TMB/Fe^{2+}/ PF127/GOx hydrogel for 12 h and 24 h.

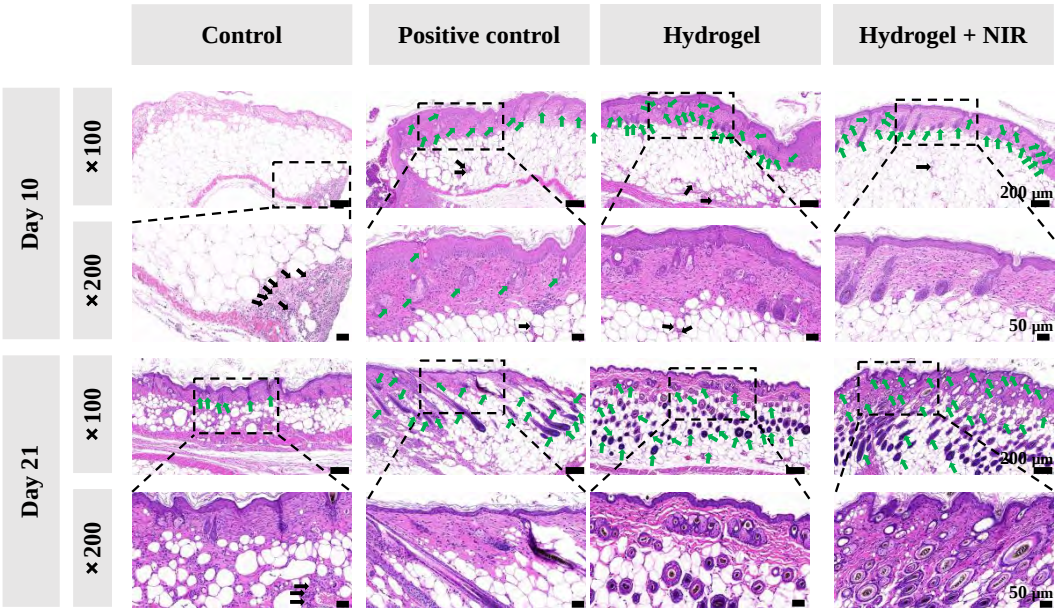

Figure S15. H&E staining of the wound regenerated tissues of mice on the 10th and 21st day after treatment. The green arrows represent hair follicles and black arrows reprensent inflammatory cells.

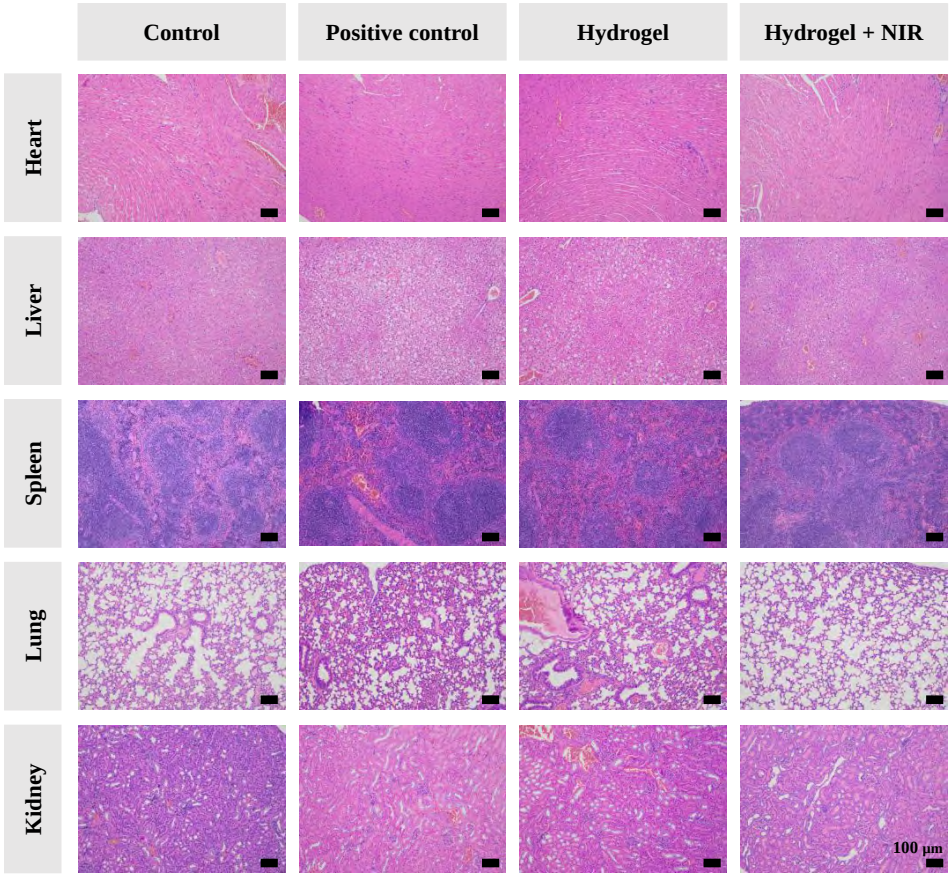

Figure S16. H&E staining of the major organs of infected mice on the 12th day after treatment.

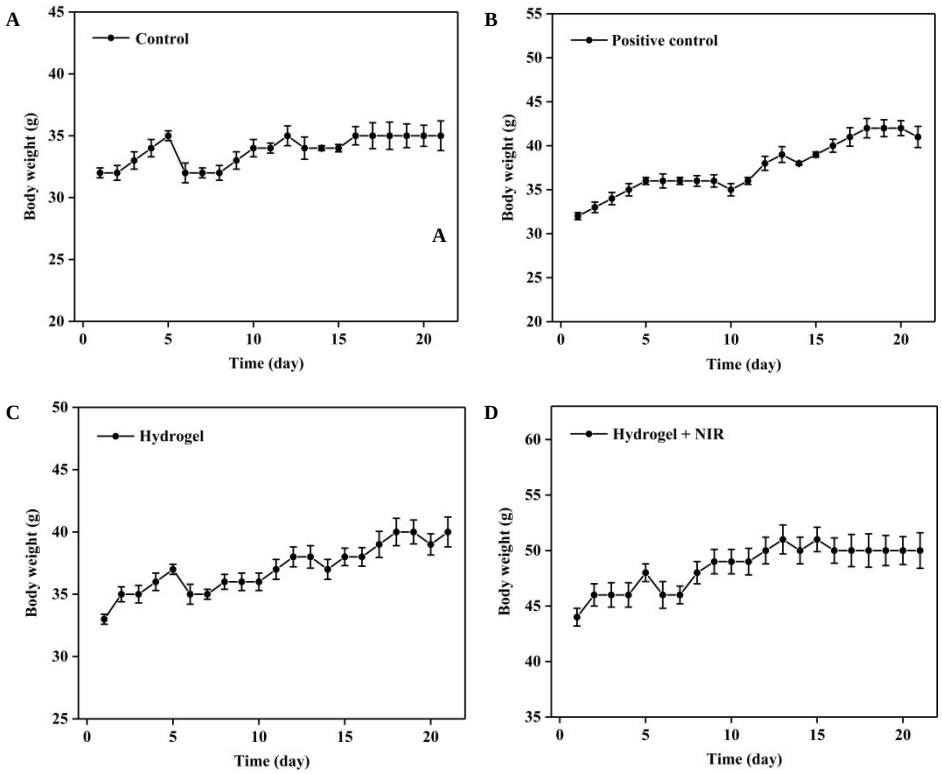

Figure S17. Weight changes of the mice during treatment.

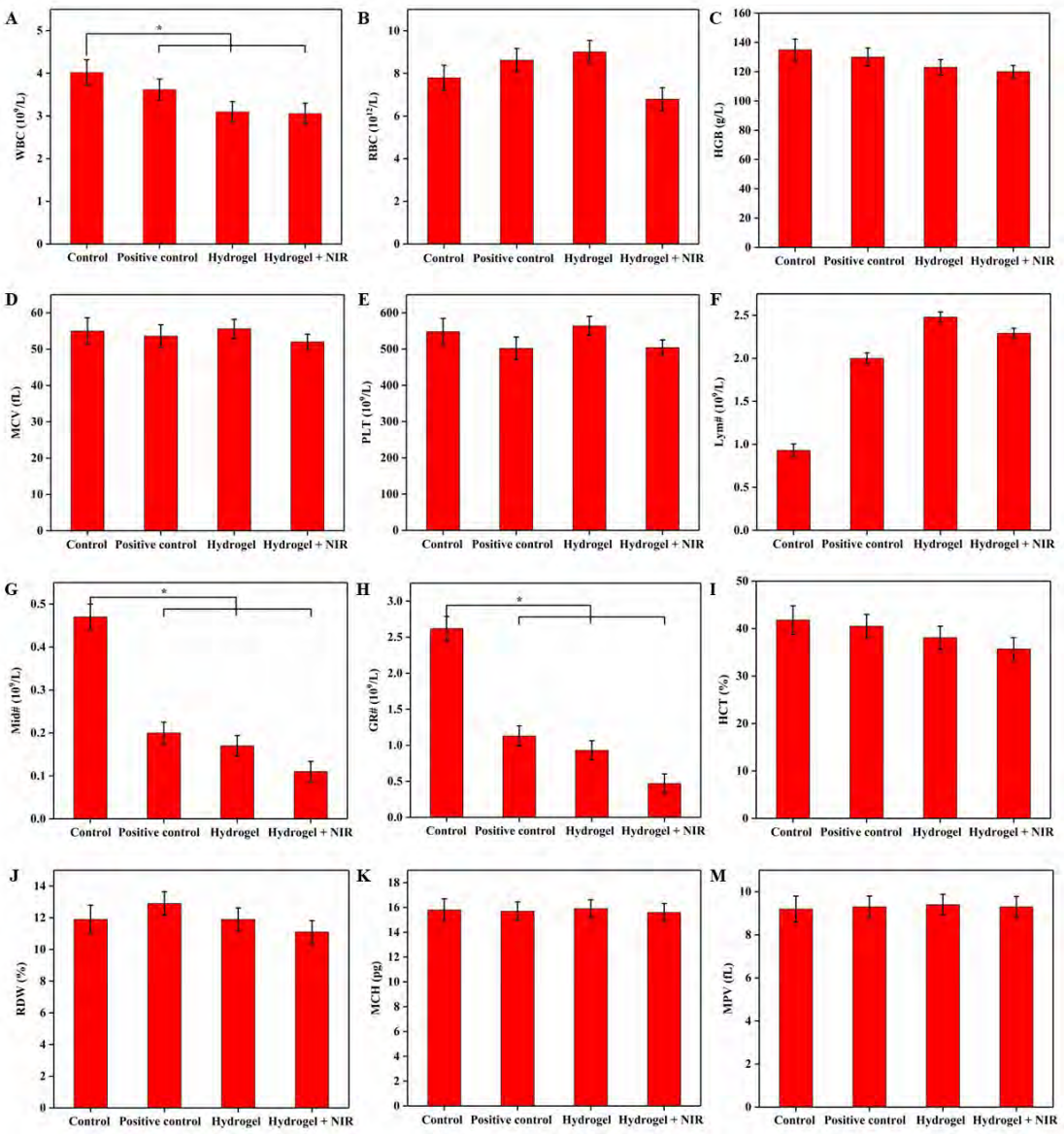

Figure S18. Biochemical analysis of the mice on the 21st day after treatment: (A) WBC, (B) RBC, (C) HGB, (D) MCV, (E) PLT, (F) Lym#, (G) Mid#, (H) GR#, (I) HCT, (J) RDW, (K) MCH, and (M) MPV.